POLITECNICO DI TORINO
Repository ISTITUZIONALE

Impact dynamics of tool steel penetrators

(Article begins on next page)

04 August 2020

POLITECNICO DI TORINO

Ph.D.
in Management, Production and Design

Ph.D. Thesis

Impact dynamics of tool steel penetrators

Giovanni Di Benedetto

Relatore

Prof. Giorgio Scavino

2017

Index

Introduction

In the last few years, there has been an increasing interest in the solution of issues relating to impacts.

Real examples of this type of loading may be found in the fields of tool design, foundry, machine shop operations, protection, vehic1e accidents, and in many other areas.

However, the analysis of impact phenomena has been restricted to collisions involving only simple types of geometry. The paramount reason for this limitation is the severe mathematical complexity encountered in the theoretical development of the phenomenon and of the behaviour of materials under conditions of rapidly applied stress.

The term "impact" lifted from its context comprehend a variety of meanings, including those related to such diverse fields as psychology, physics and engineering, but otherwise a pursuit in these various areas is unrelated.

This study treats only certain aspects of "physical impacts", define as the process involved in the collision of two or more objects.

Thus impact encompasses a wide range of processes as exemplified by the game of billiards, automobile accidents, air blast upon structures and eve molecular collisions.

However, the number of collisions must be restricted to a relatively small incidence, as otherwise a condition of repeated loading would prevail. Moreover, common terminology limits the term "impact" to collisions in which the mass effect of both impinging bodies must be taken into account.

The concept of impact is further differentiated from the case of static loading by the nature of its application. Forces created by collisions are exerted and removed in a very short interval of time and initiate stress waves which travel away from the region of contact. Impact of bodies with curved or pointed surfaces is accompanied by penetration of one member into the other. On the other hand, static loading is regarded as a series of equilibrium states and requires no consideration of accelerating or wave effects. Rapid loading is usually not produced by means of a collision, and normally involves longer loading times than found in impact processes. The transient nature of the stresses generated by static (or rapid) loading may thus frequently be neglected.

Also in this technological field, efficiency, health protection and environmental sustainability are essential properties for the success of any product.

In the last few years we have generally witnessed the abandonment of high performance materials that have been replaced by less efficient products, more respectful of environment or, above all, human health.

In this context we can frame, for example, the progressive abandonment of fossil fuels for renewable energy sources or the use of current industrial chemical products that, although less efficient and more expensive than the previous, ensure higher levels of safety.

Certainly, this kind of improvements has to be also economically sustainable both for the production and for the market.
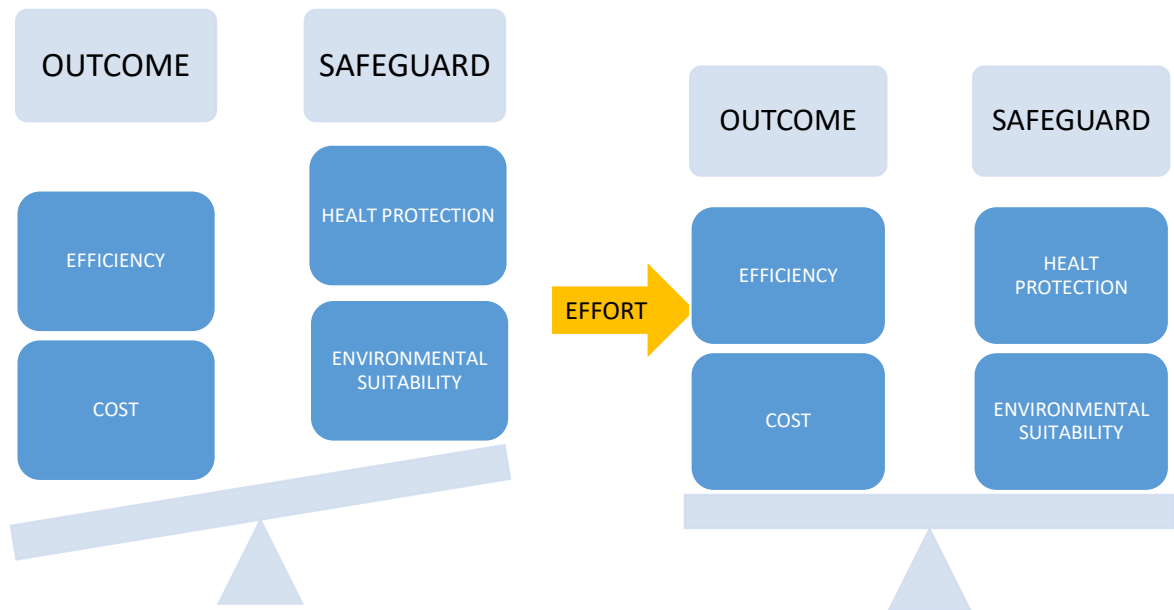
Figure 1: Current trend in balance of basic properties of the products

In particular, this study is focused on the investigation of the impact behaviour of particular types of tool steel and their fracture mechanics to understand the limit of this material in the technology of inertial perforation. In this field, the substitution of dangerous materials currently in use, having particular characteristics of resistance, presents peculiar problems for the cost of alternative efficient products.

In addition to the punching of metal materials for industrial applications, the technology of inertial penetration is widely used in the military field. This application generated one of the most important causes of environmental pollution in the theaters of war with the use of depleted uranium shells for armour piercing ammunition. Despite the use of alternative materials is a common interest to all nations and factions involved in various conflicts ongoing, the replacement of depleted uranium for this application remains very hard for the cost, the biodegradability and the efficiency of untraditional materials.

In both fields, industrial and military, the inertial penetration requires the use of very expensive alternative materials and, in any case, these materials do not ensure the operator safety.

All tests and trials of this study were performed using ballistic penetrators. This method gave us the possibility to reproduce the inertial impact phenomenon without other external contribution that could distort or falsify the results.

1   Chapter I – State of art

1.1   Inertia and evolution of the concept of inertial motion

As it is known, the inertia is the resistance of any physical object to any change in its state of motion, including changes to its speed, direction or state of rest. It is the tendency of objects to keep moving in a straight line at constant velocity. The principle of inertia is one of the fundamental principles of classical physics that are used to describe the motion of objects and how they are affected by applied forces. Inertia comes from the Latin word "*iners*", meaning idle, sluggish. Inertia is one of the primary manifestations of mass, which is a quantitative property of physical systems.

Prior to the Renaissance, the most generally accepted theory of motion in Western philosophy was based on Aristotle's theory who said that, in the absence of an external motive power, all objects would come to rest and that moving objects only continue to move so long as there is a power inducing them to do so. Aristotle explained the continued motion of projectiles, which are separated from their projector, by the action of the surrounding medium, which continues to move the projectile in some way. Aristotle concluded that such violent motion in a void was impossible.

It was a good description of the phenomenon but now we know that it was incorrect.

It has been thoroughly described by Newton in the 17th century with its Law of Inertia. In fact, according to this theory, an object will stay at rest or stay in motion (i.e. "maintain its velocity" in modern terms) unless acted on by a net external force, whether it results from gravity, friction, contact, or some other source: an object at rest stays at rest and an object in motion stays in motion with the same speed and in the same direction, unless acted upon by an unbalanced force.

The motion of a body due to no forces at all is defined *Inertial Motion*, thus resulting in straight line motion at constant speed.

All tests performed during this study could be considered, apart from the negligible effect of friction forces with the air, executed taking the advantage of the inertial motion of the impacting body. This strategy ensures that we operate in the absence of external forces that could interfere with the analyzed phenomena.

1.2 Impacts

Situations involving impact - the collision of two or more solid bodies - are currently receiving widespread attention. Traditionally, the prime interest in this area has been for military applications. However, advances in technology have placed such severe demands on materials behaviour under short-term loading that current interest in the response of materials and structures to intense impulsive loading centres on such problems as:

- punching;
- transportation safety of hazardous materials;
- vehicle crashworthiness;
- safety of nuclear reactor structures subjected to impact by tornado;
- aircraft collisions;
- the vulnerability of military vehicles, structures, and aircraft to impact and explosive loading;
- design of lightweight armor systems;
- erosion and fracture of solids due to liquid and solid particle impacts;
- protection of spacecraft from meteoroid impact;
- explosive forming and welding of metals.

The study of impact phenomena involves a variety of classical disciplines [1].

In the low velocity regime (< 2.0 m/s) many problems fall into the area of structural dynamics. Local indentations or penetrations are strongly coupled to the overall deformation of the structure. Frequently, the striker can be replaced, through the Hertz contact theory [2], with an equivalent load distribution acting over a given area in a given time and the analysis of the target performed using conventional structural analysis techniques. Typically, loading and response times are in the millisecond regime.

As the striking velocity increases (500 - 1500 m/s) the response of the structure is dominated by the behaviour of the material within a small zone (typically 2-3 punch diameters) of the impact area. A wave description of the phenomenon is appropriate and the influences of velocity, geometry, material constitution, strain rate, localized plastic flow, and failure are manifest at various stages of the impact process. Typically, loading and reaction times are on the order of microseconds.

Still further increases in impact velocity (2000 - 3000 m/s) result in localized pressures which exceed by an order of magnitude the strength of the material. In effect, the colliding solids can be treated as fluids in the early stages of impact.

At ultra-high velocities (> 12000 m/s) energy deposition occurs at such a high rate that an explosive vaporization of colliding materials results.

Impact phenomena can be characterized in a number of ways: according to the impact angle, the geometric and material characteristics of the target or projectile, or striking velocity.

A complete treatment of the impact response of materials and structures would demand that account be taken of the geometry of interacting bodies, elastic-plastic and shock wave propagation, hydrodynamic flow, finite strains and deflections, strain rate effects, work hardening, thermal and frictional effects, and the initiation and propagation of failure in the colliding materials. An analytical approach would not only be formidable but would also require a degree of material characterization under high stain rate loading that could not be attained in practice. Hence, much of the work in this field has been experimental. Existing FEM simulation models generally incorporate a high degree of empiricism and focus on few aspects of the impact response of solids.

This study focuses on high velocity impacts (300 - 1000 m/s).

For the sake of completeness, the basic mechanisms involved in the penetration and perforation of solids are stated in the following chapters. Emphasis is placed on solid-solid impacts where both loading and response times are in the sub-millisecond regime. No account is given of the impact response of composite materials.

1.3   Description of the inertial perforation phenomenon

The perforation phenomenon of a sheet steel by a punch is generally very quick and is commonly carried out with the use of higher performance materials of those which must be pierced and, in any case, employing a considerable quantities of energy.

These conditions make it difficult to define what are the important aspects of the phenomenon and the main characteristics of the materials used for punching.

The subject of penetration and perforation of solid bodies has been of interest in the military field and has recently also commended attention in a number of industrial problems:

– penetration may be defined as the entrance of a punch into a steel sheet without completing its passage through the body [3]. This involves either embedment or rebound of the striker and the formation of a crater in the sheet;

– perforation implies the complete piercing of a sheet.

Such processes occur in a time frame of several to several hundred microseconds. Sheets and punches are severely deformed during such encounters.

The complicated mechanism encountered in these processes have not yet been completely explained, although a large body of empirical knowledge in the field of terminal ballistics has been collected over the years.

For purposes of this discussion, consider the events which occur in punch and steel sheet during impact (or in projectile and target) and consider the punch (or projectile) to be in the form of a long rod, generally cylindrical in shape, with conical, ogival, hemispherical or flat nose. When such a impacting body strikes a target, strong compressive waves propagate into both elements. The initial compression wave is followed quickly by a release wave because; when it reaches the free boundary, an additional release wave is generated. If the combination of load intensity (tensile) and duration exceeds a critical value for the target material, failure will be initiated.

The steel sheet are best classified following the definitions of Backman and Goldsmith [3]. A target sheet is said to be:

a. semi-infinite if there is no influence of the distal boundary on the penetration process;
b. thick if there is influence of the distal boundary only after substantial travel of the punch / projectile into the sheet;
c. intermediate if the rear surface exerts considerable influence on the deformation process during nearly all of the penetrator motion;
d. thin if stress and deformation gradients throughout its thickness do not exist.

This study focuses on thin steel sheets.

Impacted materials may fail in a variety of ways, the actual mechanism depending on such variables as material properties, impact velocity, projectile shape, method of target support, and relative dimensions of punch and steel sheet (or projectile and target). Figure 2, adapted from Backman and Goldsmith [3], shows some of the dominant modes for thin and intermediate thickness targets.
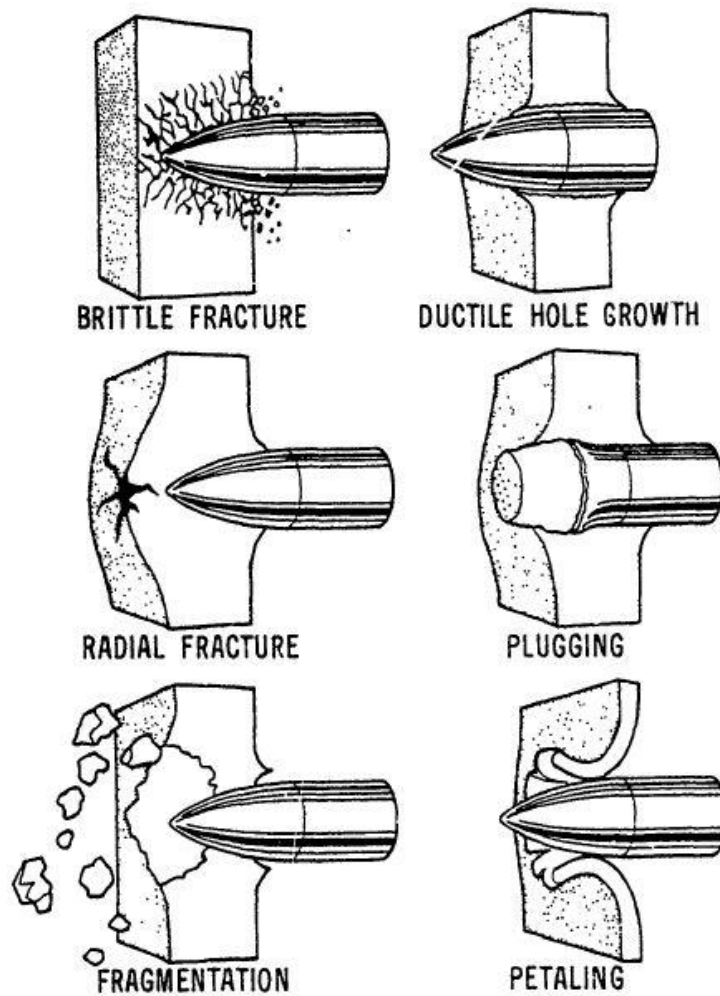
Figure 2: Failure modes in impacted plates

Plugging failure has been studied extensively, both analytically and experimentally. Impact by a blunt or hemispherically-nosed striker on a finite thickness target at a velocity close to the ballistic limit (the minimum velocity required for perforation) results in the formation of a nearly cylindrical slug of approximately the same diameter as the striker which is set in motion by the projectile.

As we can see after, the test performed in this study made only plugs.

In this study, plugging perforation of a rigid plate is very important in because, as we said above, the plugging of a finite thickness target happens at a velocity close to the ballistic limit (the minimum velocity required for perforation).

We preferred to use the word "rigid" rather than "brittle" (that has a meaning of little resistant) to indicate a material with a high tensile strength, but with a small breaking strain limit, practically coinciding with the elastic limit. It is the opposite concept of "plastic" or "ductile". When the material arrive to the elastic limit, the breaking occurs without passing through the elastic phase. It is, obviously, the phenomenon schematisation.

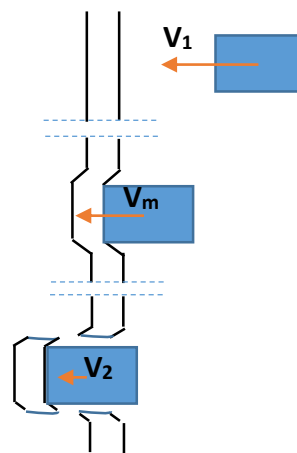The plugging perforation is schematically shown in figure 3:

Figure 3: Plugging

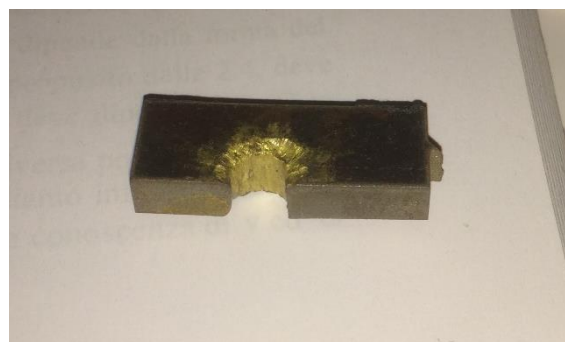A real case of plugging perforation is shown in figure 4:

Figure 4: Plugging

During the impact, a part of the plate is in shearing stress; when the elastic limit is reached, there is the breaking with the detachement of a "plug" o material that s dragged away by the punch.

As we said above, the impact creates a compression wave that propagates in the target at the speed c + v (sum of the speed of sound and the speed of the punch – Figure 5):
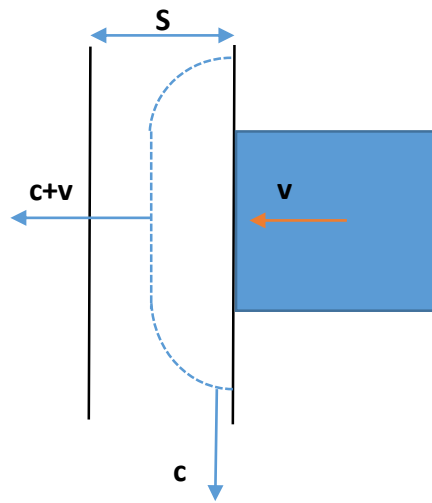

Figure 5: Progress of a plane shock wave

Considering the global nature of the phenomenon, we can use the average speed of the punch during the perforation:

$$v_m = \frac{v_1 + v_2}{2} \tag{1.1}$$

In this case, the wave crossing time within the material (Δt) is:

$$\Delta t = \frac{S}{c + v_m} \tag{1.2}$$

Instead, the wave path space in the radial direction (Δr) is:

$$\Delta r = c \cdot \Delta t = S \cdot \frac{c}{c + v_m}$$
(1.3)

Since (v_m) is normally much smaller than (c), the propagation in radial and longitudinal directions have the same size (Figure 6):
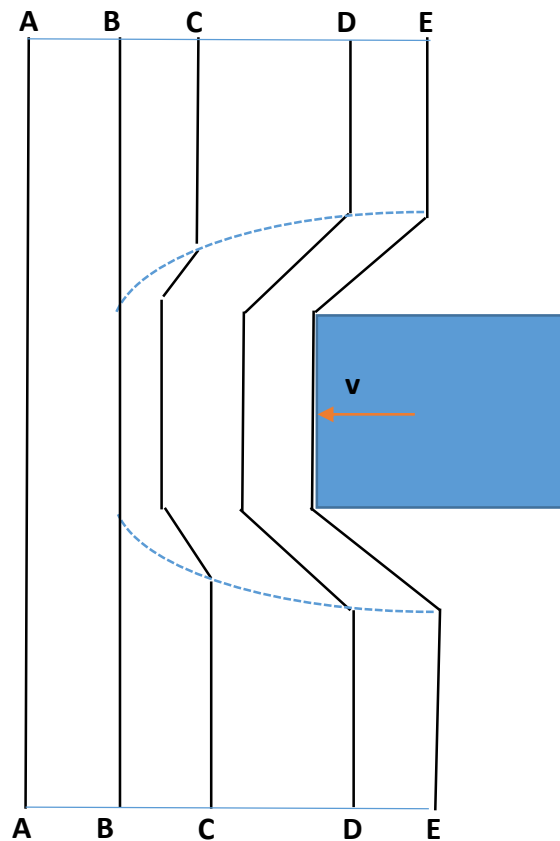

Figure 6: Progress of deformation

The figure above, while not considering the effect of compression wave reflection, helps us to outline the plugging phenomenon.

Outside the wave, the thicknesses between AA and BB have not undergone any deformation. Inside the wave, the thicknesses between BB and EE are gradually deformed until their shear breaking point, after which the material yields.

Assuming that the crack develops to an average radius X, the resistance to motion of the punch created by the flat material is as follows:

$$R_S = K_1 \frac{1}{2} \tau_{max} \cdot 2 \cdot \pi \left(r + \frac{\Delta r}{2} \right) S$$

$$\text{and}$$

$$R_C = K_2 \frac{1}{2} \sigma_{max} \cdot \pi \left(r + \frac{\Delta r}{2} \right)^2$$

(1.4)

where:

R_S = Shear resistance. It influence the punch motion for the time Δt;

R_C = Compression resistance. It influence the punch motion for the time Δt;

K1 and K2 are experimental factors;

½ take into account the assumption of working in elastic field.

Now we can write the theorem of momentum, under the assumption that the plug mass have, after the impact, the punch speed:

$$m_1 \cdot v_1 - (R_S + R_C)\Delta t = (m_1 + m_2)v_2$$

(1.5)

where:

$m_1 \cdot v_1$ = momentum of punch before the impact;

$(m_1 + m_2)v_2$ = momentum of plug and punch after the impact;

$m_2 = \rho \cdot \pi (r + \frac{\Delta r}{2})^2 S$ = mass of the plug;

½ take into account the assumption of working in elastic field.

or:

$$v_2 = \frac{m_1 \cdot v_1 - (R_S + R_C)\Delta t}{(m_1 + m_2)}$$

(1.6)

1.3.2 Petalling perforation

Petalling can be considered a typical perforation mode for thin and ductile plates.

For ductile material we intend a material with high breaking elongation, that is capable of undergo high plastic deformation field (the breaking work is mostly in plastic field and the elastic field work is practically negligible).

Where the material is deformed beyond its elongation limit, there is the formation of the petals, due to the enlargement of the punch hole, and cracks due to bending of the plate.

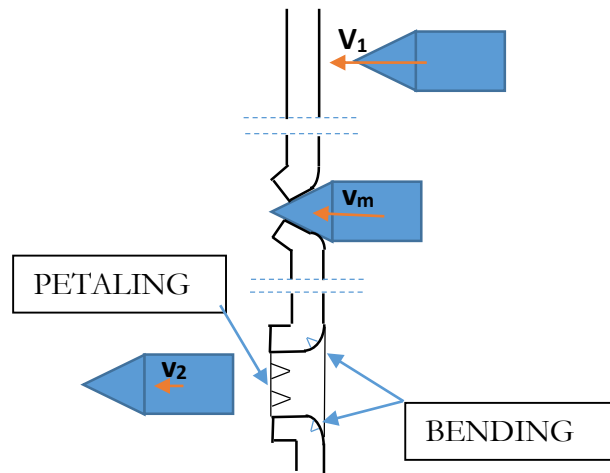The petalling perforation is schematically shown in figure 7:

Figure 7: Petalling

A real case of petalling perforation is shown in figure 8:

Figure 8: Petalling

The main works involved are as follows:
  – work of enlargement of the punch hole;
  – work of bending.

1.3.3 Spalling (or fragmentation)

It is a characteristic phenomenon, which occurs especially when they occur some concomitant conditions:

a. the plate material has a tensile strength less than the compressive;
b. the punch penetration is not very deep or is completely absent (splash);
c. the thickness of the plate is enough to prevent the perforation, but not so large to prevent the phenomenon;
d. the plate material is rigid (like the material of plugging): small breaking strain limit.

A real case of spalling is shown in figure 9:

Figure 9: Spalling

Only for the present dissertation, we will refer to the typical case of no penetration, i.e. "splash" of the punch against the plate.

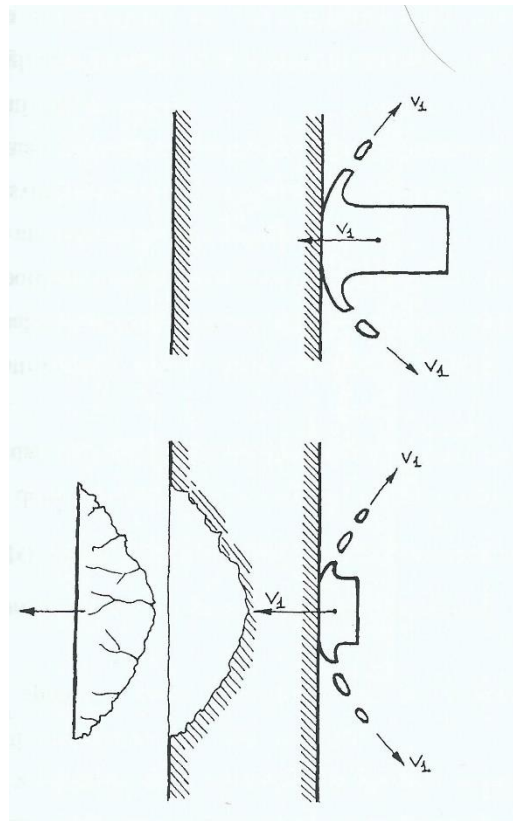Phenomena that can be observed are indicated in the figure 10:

Figure 10: Spalling

On the front face of the plate there is any permanent deformation. On the contrary, on the rear side, it produces a large crater, with projection of detached material.

It is a phenomenon relating to the propagation of pressure waves within the material that will be extensively discussed in the next paragraph, but not difficult to understand.
In the point of impact is generated a pressure wave that propagates in a hemispherical manner inside of the plate, thereby reducing its intensity approximately inversely proportional to the distance (radius).
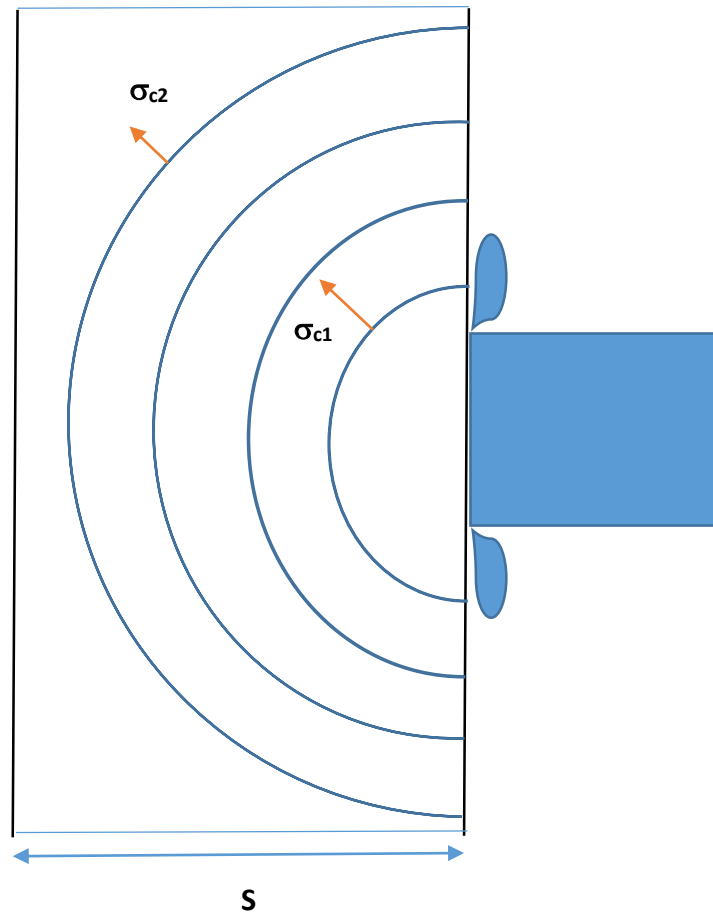
Figure 11: Progress of a spherical shock wave

In this phase it is difficult to produce the material breaking, because there are only compression waves.

When these waves arrive at the edge of the material are reflected as a tensile wave (changing sign but maintaining the module), as showed below:

Figure 12: Reflection of a spherical shock wave

In this case, if the reflected wave is greater than the breaking strain limit, there is the breaking of the material that forms a crater on its rear part.

1.4 Stress waves in solids

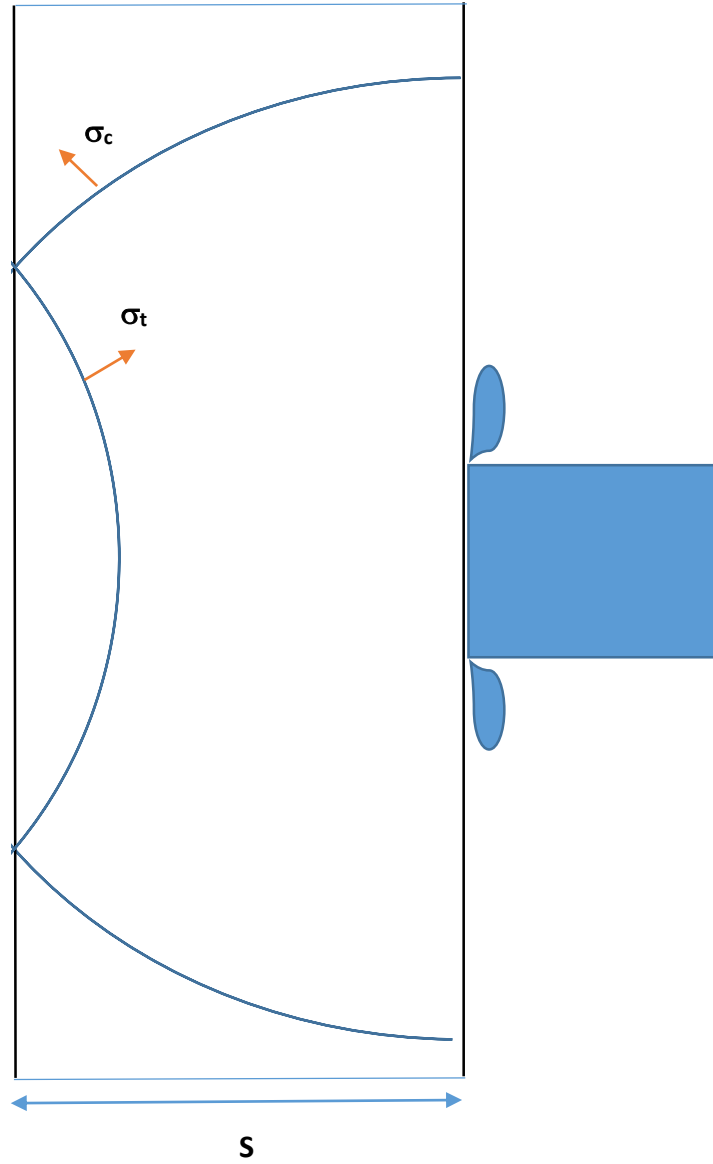A disturbance exerted on some physical quantity in a limited region space, is propagated in the surrounding space with modes that depend normally the type of perturbation and the characteristics of the material.

In the course of this propagation, part of mechanical energy is converted into heat, through different mechanisms indicated, in general, such as internal friction. These phenomena introduce such complexity in the mathematical models that describe wave motion, to make them "intractable". And this is the reason why these effects are neglected in most treatments without affecting their validity [1].

1.4.1 Wave equation

To make conceptually clear and more intuitive the formulation of the equation of the waves, it is necessary, at least initially, to limit the discussion to the one-dimensional wave propagation.

Consider the problem of a disturbance that propagates in the X direction with respect to a fixed reference system, as shown in Figure 13 and examine the forces acting on a mass element

$$dm = \rho \cdot dx \cdot A$$

Suppose we limit the analysis to the case of small deformations and small displacements.

The one-dimensional equation of motion for longitudinal vibration of a rod is derived from a force balance across an element dx:
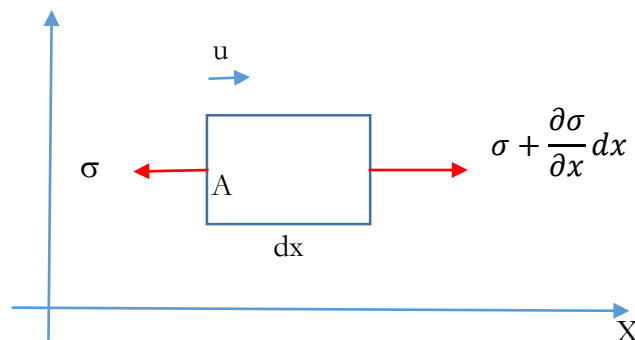

Figure 13: Free body diagram of element of length dx

Where:

$\sigma = \frac{F}{A}$ is the <u>stress</u> in the x-direction as positive in tension;

A   is the <u>section area</u>;

u   is the <u>x-displacement</u>.

For the conservation of momentum:

$$\frac{\partial \sigma}{\partial x} = \rho \frac{\partial v}{\partial t} \qquad (1.7)$$

Where:

the v is the <u>particle velocity</u>, defined as and:

$$v = \frac{\partial u}{\partial t} \qquad (1.8)$$

Considering that the <u>longitudinal strain</u> in the x-direction is ε, defined as:

$$\varepsilon = \frac{\partial u}{\partial x} \qquad (1.9)$$

and assuming that stress is a single value function of strain, i.e.:

$$\sigma = \sigma(\varepsilon) \qquad (1.10)$$

we obtain the <u>wave equation</u> for one-dimensional motion:

$$dF = AE \frac{\partial^2 u_x}{\partial x^2} = \rho A \frac{\partial^2 u_x}{\partial t^2}$$

Or   (1.11)

$$c_0^2 \frac{\partial u_x}{\partial x^2} = \frac{\partial^2 u_x}{\partial t^2}$$

Where:

A is the section;

dF is the differential force across the element;

c_0 is the wave velocity:

$$c_0^2 = \frac{E}{\rho} \qquad (1.12)$$

The solution of equation (1.11) is on the form

$$u_x = f(x - c_0 t) + g(x + c_0 t) \qquad (1.13)$$

which represent two superposed waves traveling in the positive and negative directions.
Successive differentiations of equation (1.13) give us:

$$\varepsilon_x = \frac{\partial u_x}{\partial x} = f'(x - c_0 t) + g'(x + c_0 t)$$

$$\sigma_x = E \cdot \varepsilon_x = E \cdot [f'(x - c_0 t) + g'(x + c_0 t)] \qquad (1.14)$$

$$v = \frac{\partial u_x}{\partial t} = c_0 \cdot [-f'(x - c_0 t) + g'(x + c_0 t)]$$

When the wave travels only in one direction, the equation (1.14) show that:

$$|\sigma_x| = \rho c_0 v \qquad (1.15)$$

The solutions of equation (1.11) are based, however, on the assumption that the stress-train curve is concave down, so that shock waves do not form. Shock waves will be discussed later in this chapter.

1.4.2 Impact stress

To find the intensity of the generated stress in an impact, reference may be the event, represented in Figure 14, of a rigid wall which, at time t = 0, impacts, in speed v = v_0, a bar or a disc at rest:
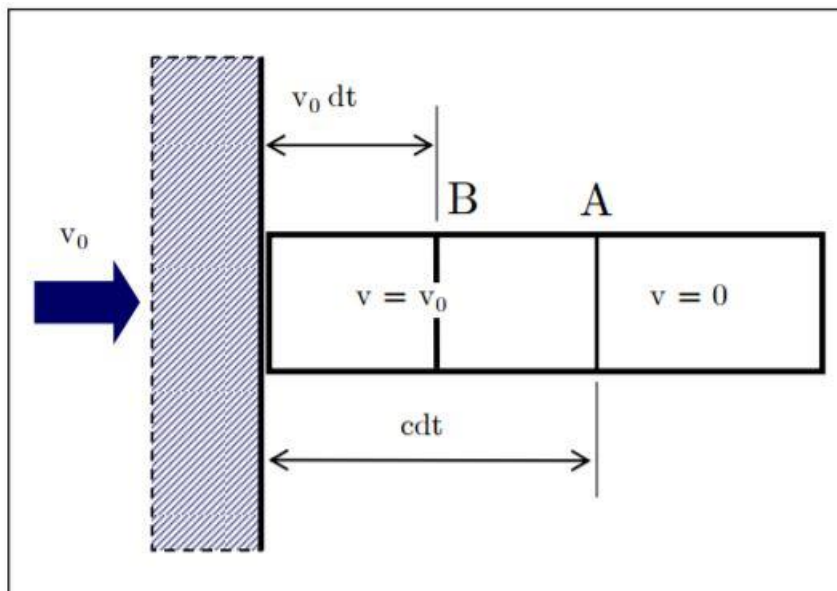

Figure 14: Schematic of rigid wall impacting rod at velocity v_0

In the interval of time dt, the bar will deform up to plan B which is at $v_0 \cdot dt$ from their original position. The disorder, which brings the speed of the particles at v_0, will travel, in the same time interval, until the plane A, for a distance equal to $c \cdot dt$, where c is the wave velocity.

If we denote by σ the compression strain which is generated between the impactor and the A_0 section bar, the impulse generated by the interval dt is equal to σ A_0 dt.

The momentum of the bar, initially at rest, is equal to $\rho \cdot A_0 \cdot cdt \cdot v_0$, (product velocity and mass of the particles compressed between the initial surface and the plane A).

Equating the impulse to the variation of the amount of motion, is obtained:

$$\sigma = \rho c v_0 \qquad (1.16)$$

If the initial state of stress and speed is not zero, the quantities σ and v_0 must be replaced by their corresponding variations Δσ and Δv, which lead to the expression more general:

$$\Delta\sigma = \rho c \Delta v \qquad (1.17)$$

1.4.3   Wave reflection

Any elastic wave will be reflected when it reaches a free surface of the material in which it is traveling. The simplest case occurs when the wave strikes the surface normally. In a longitudinal wave, since the stress normal to the surface at the surface must be zero, the reflected pulse must be opposite in sense to the incident pulse (compression reflected as tension and vice versa) and then, at the free boundary, the net stress must be zero:

$$\sigma_{NET} = \sigma_I + \sigma_R = 0 \qquad \text{at}$$
$$\text{x=l} \qquad (1.18)$$

Where σ_I and σ_R are the incident and reflected stresses.

Since the stress in given by $\sigma = E \cdot \varepsilon = E(\partial u / \partial x)$, the stress will be:
$$\sigma_{NET} = E[f'(l - ct) + g'(l + ct)] = 0$$
$$\text{or} \qquad (1.19)$$
$$f'(l - ct) = -g'(l + ct)$$

Hence, the shape of the reflected pulse is the same as the shape of the incident pulse, but opposite in sing.

The net particle velocity can also be found by superposition:

$$v_{NET} = v_I + v_R = \frac{\partial u_I}{\partial t} + \frac{\partial u_R}{\partial t}$$

On the surface: $x = l$

$$v_{NET} = c(-f' + g') = 2cg'$$

(1.20)

Hence, the particle velocity and also the displacement in a region where the incident and reflected pulse overlap are twice that for either pulse.

A convenient technique for visualization of the behaviour of stress pulses at an interface, Figure 15, is proposes by Zukas [1] and relies on the linearity of the wave equation which permits superposition of solutions.

There are a the real pulse (with red crosshatch) and a phantom pulse (ghost) with the same shape but with opposite signs, traveling toward the surface with the same velocity and striking it at the same time.

At the surface, the incident wave pass out of the material and the phantom wave pass into the material without any distortion.

We can see in figure 15 that, during the overlap, the net stress will be 0 (but we have to remark that particle speeds are double). After the superposition of the pulses, only the phantom is continuing its route into the material (now it is the real but with opposite sign).
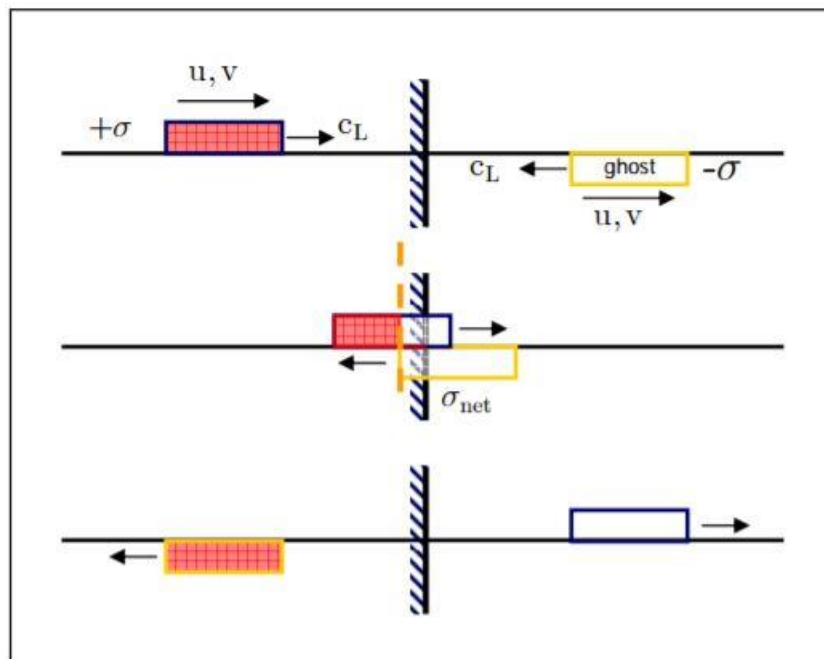

Figure 15: Reflection of a longitudinal wave on a free surface perpendicular to the direction of wave propagation

On a fixed surface, instead, as illustrated in Figure 16, the speed and the displacement should be zero and, following the same procedure, we can write for the particles velocity:

$$v_{NET} = -cf'(l - ct) + cg'(l + ct) = 0$$

or (1.21)

$$cf'(l - ct) = cg'(l + ct)$$

and for the stress:

$$\sigma_{NET} = E(\varepsilon_I + \varepsilon_R) = E\left(\frac{\partial u_I}{\partial x} + \frac{\partial u_R}{\partial x}\right)$$
$$= E[f'(l - ct) + g'(l + ct)] \qquad (1.22)$$
$$\text{On the surface: } x = l$$
$$\sigma_{NET} = 2Ef'(l - ct)$$

Therefore, on a fixed surface, the wave reflection create, a double net stress and zero net displacement and particle velocities.
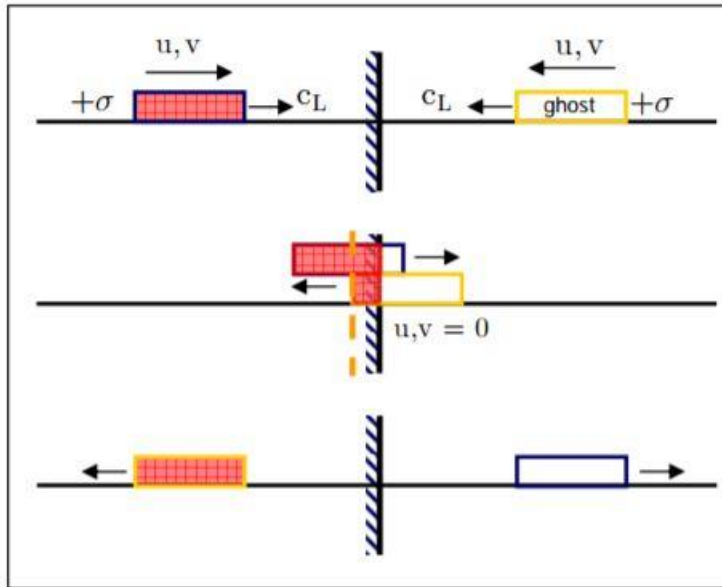

Figure 16: Reflection of a longitudinal wave on a fixed surface perpendicular to the direction of wave propagation

1.4.4   Shock waves

The following is a brief, simplified summary of shock-wave propagation and relies primarily on the reports [2] and [5].

Historically, work on shock waves has been done with plate geometries. Plate impact situations generate a state of uniaxial strain but three-dimensional stress, whereas in bar

experiments a state of uniaxial stress was assumed in the one-dimensional approximations. The reason for the change in geometry was the necessity to obtain higher stress amplitudes and higher strain rates. Recall that in the bar impact experiments, plastic flow near the impact end introduced three-dimensional effects (radial inertia, heating) so that one- dimensional theory applied only at points far away from the point of application of the load. With increasing striking velocity a three-dimensional theory is required for complete analysis of experimental results. That, unfortunately, is beyond current capability. Plate geometry offers the opportunity to study materials behaviour at higher loads and shorter times while offering again the simplicity of a one-dimensional analysis, this time for uniaxial strain. However, just as bar theories neglected lateral inertia, plate impact analyses neglect effects of thermomechanical coupling, which can be significant at strains exceeding 30%. Much of the initial work assumed hydrodynamic behaviour of the material. However, an elastic precursor can produce significant volumetric strain. An elastic unloading wave can significantly change the local state of the material before the arrival of a plastic wave so that finite elastic and plastic effects may need to be accounted for.

The conventional uniaxial stress-strain curve, as depicted by the idealized models of Figure 17, does not adequately represent the state of stress and strain to which a material is subjected under shock loading. Therefore the quantities associated with such curves (elastic modulus, yield strength, ultimate strength, and elongation) are not by themselves appropriate to describe the relative behaviour of materials.
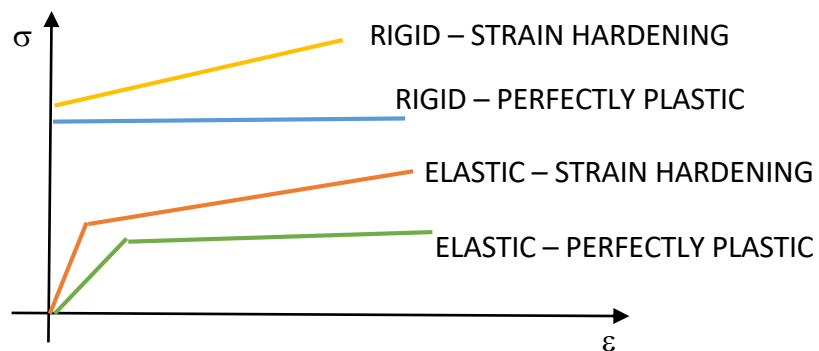

Figure 17: Characteristic uniaxial stress-strain curves

lf we visualize a situation where deformation is restricted to one dimension, an in the case of plane waves propagating through a material where dimensions and constraints are such that the lateral strains are zero, the characteristic stress-strain curve takes on the form shown in Figure 18. This situation is commonly referred to as uniaxial strain.
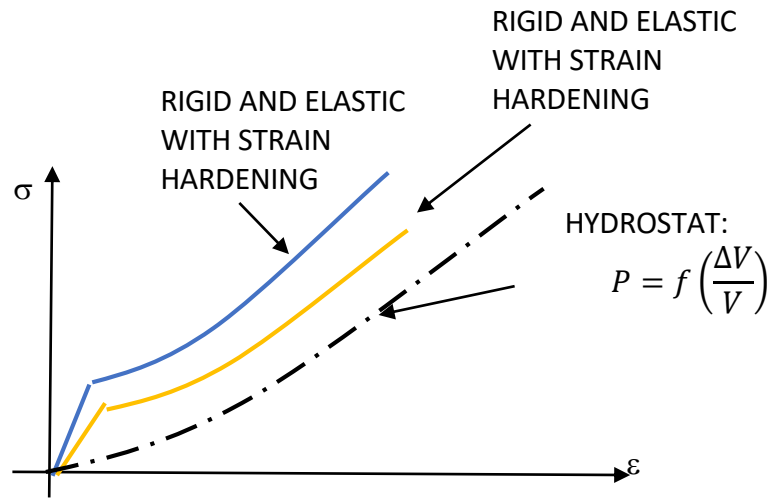
Figure 18: Stress-strain curves for uniaxial strain

To understand why these changes occur, consider the stress-strain relationship for one-dimensional deformation. In the general case (strains <30) the three principal strains can be divided into an elastic and a plastic part:

$$\begin{cases} \varepsilon_1 = \varepsilon_1^e + \varepsilon_1^p \\ \varepsilon_2 = \varepsilon_2^e + \varepsilon_2^p \\ \varepsilon_3 = \varepsilon_3^e + \varepsilon_3^p \end{cases} \tag{1.23}$$

Where the superscripts e and p refer to elastic and plastic, respectively, and the subscripts are the three principal directions.

In one-dimensional deformation:

$$\begin{cases} \varepsilon_1 = \varepsilon_1^e + \varepsilon_1^p \neq 0 \\ \varepsilon_2 = \varepsilon_2^e + \varepsilon_2^p = 0 \\ \varepsilon_3 = \varepsilon_3^e + \varepsilon_3^p = 0 \end{cases} \implies \begin{cases} \varepsilon_2^e = -\varepsilon_2^p \\ \varepsilon_3^e = -\varepsilon_3^p \end{cases}$$

The plastic portion of the strain is taken to be incompressible, so that:

$$\varepsilon_1^p + \varepsilon_2^p + \varepsilon_3^p = 0$$

Which gives:

$$\varepsilon_1^p = -\varepsilon_2^p - \varepsilon_3^p = -2\varepsilon_2^p \tag{1.24}$$

since $\varepsilon_2^p = \varepsilon_3^p$ due to symmetry.
From (1.24) we have that:

$$\varepsilon_1^p = 2\varepsilon_2^e \tag{1.25}$$

so, that the total strain ε_1 may be written as:

$$\varepsilon_1 = \varepsilon_1^e + \varepsilon_1^p = \varepsilon_1^e + 2\varepsilon_2^e \tag{1.26}$$

The elastic strain in terms of the stresses and elastic constants is given by:

$$\begin{cases} \varepsilon_1^e = \dfrac{\sigma_1}{E} - \dfrac{v\sigma_2}{E} - \dfrac{v\sigma_3}{E} = \dfrac{\sigma_1}{E} - \dfrac{v(\sigma_2 + \sigma_3)}{E} \\[2mm] \varepsilon_2^e = \dfrac{\sigma_2}{E} - \dfrac{v\sigma_1}{E} - \dfrac{v\sigma_3}{E} = \dfrac{\sigma_2}{E} - \dfrac{v(\sigma_1 + \sigma_3)}{E} \\[2mm] \varepsilon_3^e = \dfrac{\sigma_3}{E} - \dfrac{v\sigma_2}{E} - \dfrac{v\sigma_1}{E} = \dfrac{\sigma_3}{E} - \dfrac{v(\sigma_2 + \sigma_1)}{E} \end{cases} \tag{1.27}$$

Combining (1.26) and (1.27) we obtain:

$$\varepsilon_1 = \frac{\sigma_1(1 - 2v)}{E} + -\frac{2\sigma_2(1 - 2v)}{E} \tag{1.28}$$

The plasticity condition for either the Von Mises or Tresca conditions for this case is:

$$\sigma_1 - \sigma_2 = Y_0 \tag{1.29}$$

Using (1.29) as the definition for σ_2:

$$\sigma_2 = \sigma_1 - Y_0$$

and inserting into (1.29) gives:

$$\sigma_1 = \frac{E}{3(1 - 2v)}\varepsilon_1 + \frac{2}{3}Y_0 = K\varepsilon_1 + \frac{2}{3}Y_0 \qquad (1.30)$$

where K=E/3(1-2v) is called the Bulk Modulus.

The most important difference between uniaxial stress and uniaxial strain is the bulk compressibility term: the stress now continues to increase regardless of the yield strength or strain hardening.
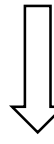For ballistic impact or other high-rate phenomena where the material does not have time to deform laterally, a condition of uniaxial strain will initially occur. Later on, as lateral deformation takes place, a condition approaching uniaxial stress may occur and the stress will decrease.

For the special case of elastic one-dimensional strain:

$$\begin{cases} \varepsilon_1 = \varepsilon_1^e \neq 0 \\ \varepsilon_2 = \varepsilon_2^e = 0 \\ \varepsilon_3 = \varepsilon_3^e = 0 \end{cases}$$

and

$$\varepsilon_1^p = \varepsilon_2^p = \varepsilon_3^p = 0$$

$$\varepsilon_2^e = 0 = \frac{(1 - v)\sigma_2}{E} - \frac{v\sigma_1}{E}$$

$$\sigma_2 = \frac{v}{(1 - v)}\sigma_1$$

And

$$\varepsilon_1 = \frac{\sigma_1}{E} - \frac{2v^2\sigma_1}{E(1 - v)}$$

or $\qquad\qquad$ (1.31)

$$\sigma_1 = E\varepsilon_1 \frac{(1 - v)}{(1 - 2v)(1 + v)}$$

Equation (1.27) shows that the slope of the elastic line in one-dimensional strain is: (1-v)E /[(1-2v)(1+v)].

When very high pressures are considered, the pressure-compressibility curve of Figure 18 (P=f(ΔV/V) where ΔV/V is the volumetric strain), also known as the Hugoniot curve, is the

only one that is considered to describe the behavior of a material. At lower pressures, such as those generated by conventional impacts, considerable deviation from the Hugoniot occurs. For example, the uniaxial strain curve corresponding to the uniaxial stress condition for an elastic, perfectly plastic material (Figure 19) is shown in Figure 20.
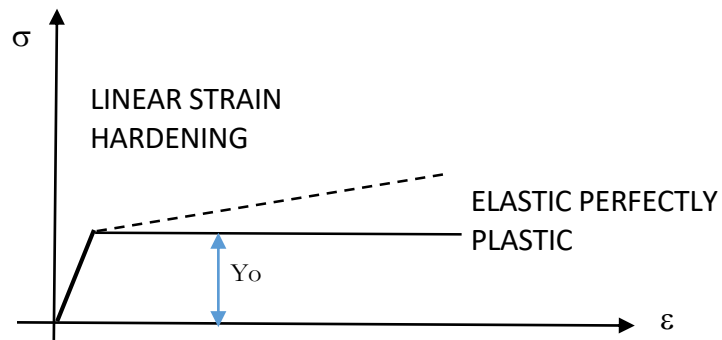

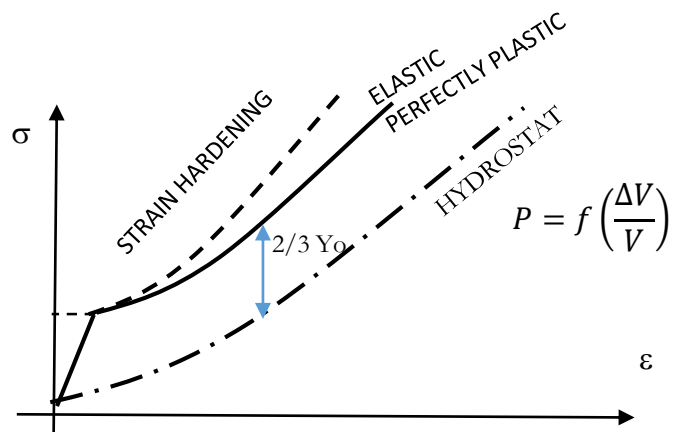*Figure 19: Uniaxial stress state for elastic, perfectly plastic material*

Figure 20: Uniaxial strain curve for elastic, perfectly plastic material

Note there:
a. The increase in modulus by a factor $(1-\nu)E /[(1-2\nu)(1+\nu)$;
b. The Hugoniot elastic limit σ_{HEL}, the maximum stress for one-dimensional elastic wave propagation (uniaxial strain);
c. The constant deviation from the Hugoniot of the stress al by $2Y_0/3$, where Y_0 is the static yield strength. If the yield strength changes in a strain-hardening material, so will the difference between the σ_1 and P curves. A typical loading cycle in uniaxial

strain for an elastic, perfectly plastic material is shown in Figure 21. Note that the reverse yielding occurs at point C. If reverse loading occurs, as in stress-wave reflection from a free surface, the line segment CD extends to the negative (tension) region below the strain axis but again different by 2Yo/3 from the hydrostat (Hugoniot), assuming tensile and compressive yield strengths are equal.
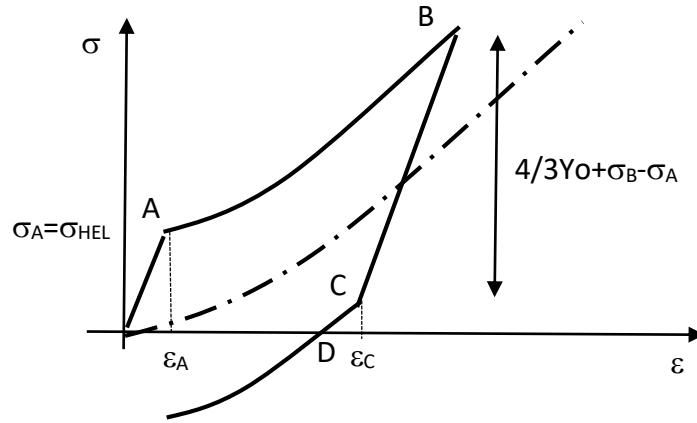

Figure 21: Loading cycle in uniaxial strain

If the magnitude of the applied stress pulse is above σ_{HEL}, two waves will propagate through the medium:

the elastic wave moving with speed:

$$c_e^2 = \frac{E(1-\nu)}{\rho_0(1-2\nu)(1-\nu)} \tag{1.32}$$

followed by a plastic wave moving with speed:

$$c_p^2 = \frac{\sigma_B - \sigma_{HEL}}{\rho_{HEL}(\varepsilon_B - \varepsilon_A)} \tag{1.33}$$

If the applied stress is of finite duration, an e1astic unloading wave is generated after removal of the load (Figure 22).
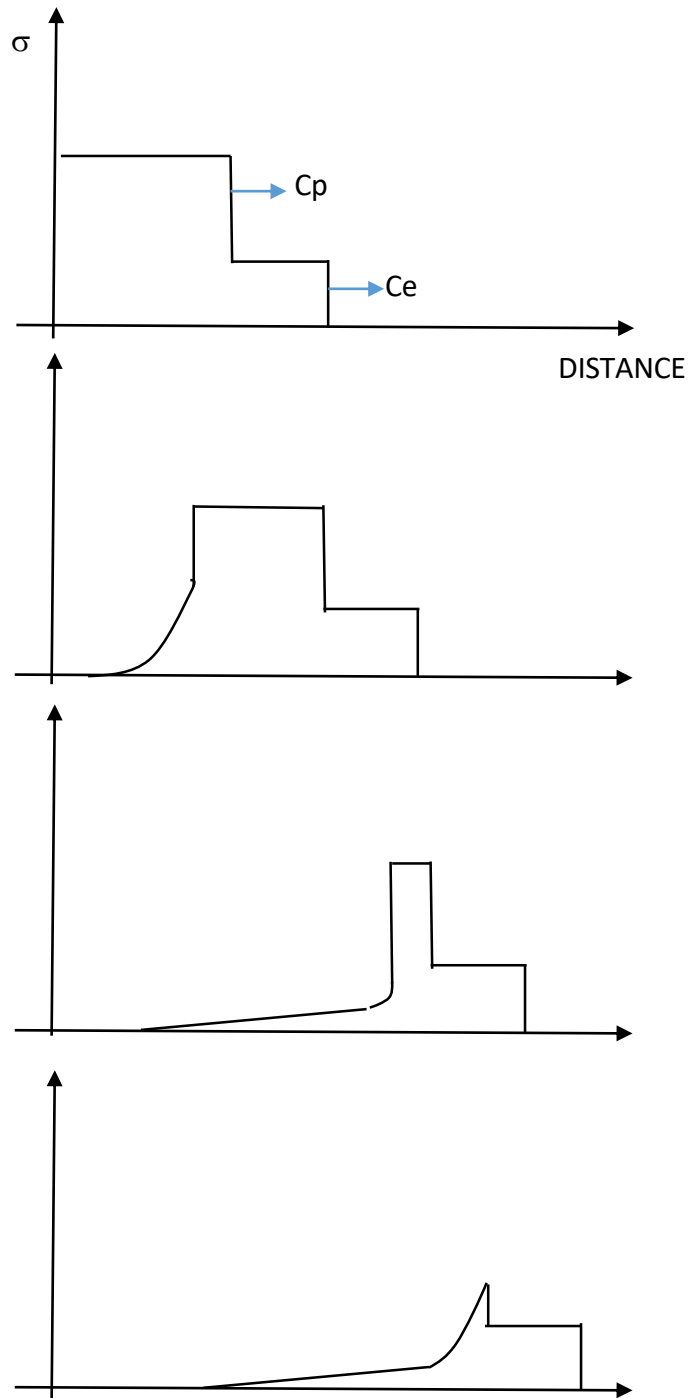

Figure 22: Plastic wave attenuation

The unloading wave travels faster than the compressive wave so that for a short duration pulse the compressive amplitude may be attenuated by unloading from the rear. The point at which this unloading occurs is called the catch-up distance and is usually defined in terms of the incident pulse thickness.

If we have a situation where $C_p > C_e$, conditions have been created for the formation of a steep plastic front. The more rapidly traveling stress components overtake the slower ones. The continuous plastic wave front breaks down and a single discontinuous shock front is formed traveling at a shock velocity U.

Across the shock front, there is a discontinuity in stress, density, velocity, and internal energy.
Shock waves will form under conditions of extremely high impulsive stress and will propagate in a material in a manner similar to the fluid dynamics situation. It becomes reasonable to consider the solid as behaving like a compressible fluid described by an equation of state. Shock-wave propagation has inherent simplifying features (simplified equation of state) analogous to the case of elastic waves (linear elastic behavior) which permits some simplified solutions for the one-dimensional strain case.

Consider Now the case of a uniform pressure P_1, suddenly applied to one face of a plate of compressible material that is initially at pressure P_0. This pulse is propagated by means of a wave traveling at velocity U_s. Application of P_1 compresses the material to a new density ρ_1 and at the same time accelerates the compressed material to a velocity U_p. Now consider a segment of the material (with unit cross-sectional area) normal to the direction of wave travel. The position of the shock front at some instant of time is indicate in figure 23 by the line AA. A short dt later, the shock front has advanced to BB while the matter initially at AA has moved to CC. Across the chock front, mass, momentum and energy are conserved.
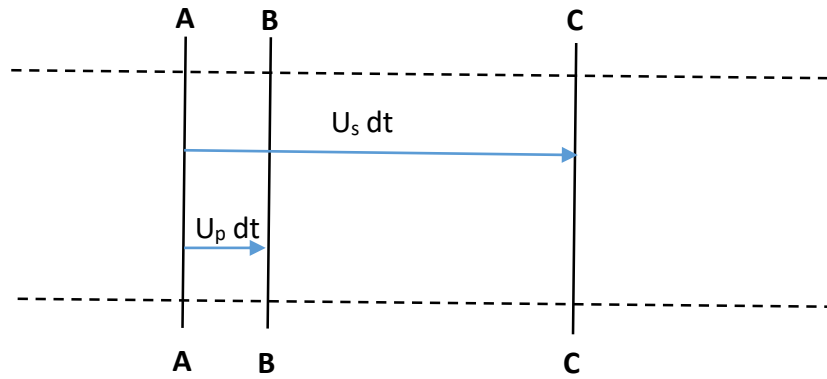
Figure 23: Stress front moving

Conservation of mass across the shock front may be expressed by noting that the mass of material encompassed by the shock wave $\rho_0 \cdot U_s \cdot dt$ now occupies the volume $(U_s - U_p) \cdot dt$ at dendity ρ_1.

$$\rho_0 U_s = \rho_1 (U_s - U_p)$$

or

$$V_1 U_s = V_0 (U_s - U_p) \tag{1.34}$$

where $V = 1/\rho$

Conservation of momentum in expressed by noting that the rate of change of momentum of a mass of material $\rho_0 \cdot U_s \cdot dt$ in time dt accelerated to a velocity U_p by a net force $P_1 - P_0$ in given by:

$$P_1 - P_0 = \rho_0 U_s U_p \tag{1.35}$$

The expression on conservation of energy across the shock front is obtained by equating the work done by the shock wave with the sum of the increase of both kinetic and internal energy of the system. Thus:

$$P_1 U_p = \frac{1}{2} \rho_0 U_s U_p^2 + \rho_0 U_s (E_1' - E_0') \tag{1.36}$$

Equations 1.34 – 1.36 contain a total of 8 parameters (ρ_0, ρ_1, P_0, P_1, U_s, U_p, E_1' and E_0'). If it is assumed that ρ_0, P_0 and E_0' are known, three equations with five unknown remain. By

eliminating U_s and U_p through 1.34 and 1.35, the resulting equation is known as the Rankine. Hugoniot relation:

$$E_1' - E_0' = \frac{1}{2}(V_0 - V_1)(P_1 + P_0) = \frac{1}{2}(\frac{1}{\rho_0} - \frac{1}{\rho_1})(P_1 + P_0) \qquad (1.37)$$

Equations 1.24 - 1.25, and either 1.36 or 1.37 are the "jump conditions" that must be satisfied by material parameters on the two sides of a shock front.

Hence the states (E_1', ρ_1, P_1) that can be achieved from an initial state (E_0', ρ_0, P_0) have been identified.

Elimination of the particle velocity from the mass and momentum equations results in an expression for the shock velocity of the form:

$$U_s^2 = \frac{1}{\rho_0^2}\frac{P_1 - P_0}{V_0 - V_1}\rho_0 U_s U_p^2 + \rho_0 U_s(E_1' - E_0') \qquad (1.38)$$

where $V_0 = 1/\rho_0$ and $V_1 = 1/\rho_1$.

Changes in pressure, density ad internal energy across a shock front can be calculated by measurement of just two parameters, the shock velocity U_s and the particle velocity U_p.

The locus of pressure-density states that are attainable by shock loading from a single initial state is called the Rankine-Hugoniot curve of a material, or simply the Hugoniot. The term is frequently applied to those curves representing any two of the five variables (pressure, density, internal energy, shock velocity and particle velocity). The assumption made in the development of the Hugoniot were one-dimensional motion, thermodynamic equilibrium ahead of and immediately behind the shock front, and neglect of material rigidity. The first can generally be met experimentally, the second will hold if thermodynamic equilibrium is achieved within a few tenths of microseconds after passage of a shock, and the third is justified for extremely high pressures (some two orders of magnitude above the yield strength of the material).

The Hugoniot curve for the solid is often fit to experimental data in the straight line form:

$$b = a + bU_p \qquad (1.39)$$

The physical reason for the good agreement with the linear relationship is not well understood. The constant a represent the wave velocity in an extended medium.

The constant b is related to the Gruneisen parameter at low pressure through:

$$b = \frac{1 + \Gamma}{2} \qquad (1.40)$$

where $\Gamma = 3\alpha K / \rho_0 C_v$

with α = coefficient of linear expansion;

          K = bulk modulus;

          C_v = specific heat at constant volume;

          ρ_0 = initial density.

When Hugoniot data for a particular material are not available, first approximation may be generated from the bulk sound speed (a) and the value of Γ at zero pressure.

Using these relationships and a constitutive equation for the material as well as the conditions of impact, is possible to infer the stress history within the interior of the material. The inverse problem, in which the material properties are to be found from the plate impact test, is equally important but is not described in this work.

1.5   Explosion welding

The knowledge of this technology will be useful to understand an important aspect of the physical phenomena occurred during the tests.

Explosion welding (EXW) is a solid state (solid-phase) process where welding is accomplished by impacting of two metals: accelerating one of the components at extremely high velocity to the other, through the use of chemical explosives (Figure 24).
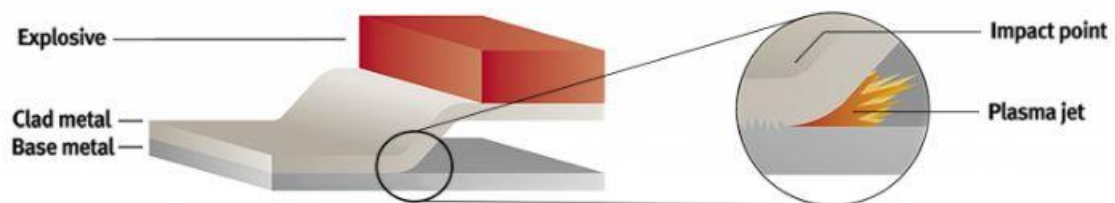

Figure 24: Explosion welding process

It is use to force two metals (also incompatible) together at high pressures.

1.5.1 Development

Unlike other forms of welding such as arc welding (which was developed in the late 19th century), explosion welding was developed relatively recently, around the middle of last century.

Since the extreme heat involved in other forms of welding did not play a role, it was concluded that the phenomenon was caused by the explosive forces acting on the shrapnel. These results were later duplicated in laboratory tests and, not long afterwards, the process was patented and put to use.

The resultant composite system is joined with a high-quality metallurgical bond. The time duration involved in the explosive welding event is so short, that the reaction zone between the constituent metals is microscopic. During the bonding process, several atomic layers on the surface of each metal become plasma. The collision angle between the two surfaces (typically less than 30°) forces the plasma to jet ahead of the collision front, effectively scrubbing both surfaces and leaving virgin metal.

The remaining thickness remains near ambient temperature and acts as a huge heat sink. Therefore, the bond line is an abrupt transition from the clad metal to the base metal with virtually no degradation of their initial physical or mechanical properties. The obvious benefit from this process is the joining of metallurgically incompatible systems. Any conventional cladding method, which uses heat, may cause brittle inter-metallic compounds to form.

This process is most commonly utilized to clad steel plate with a thin layer of corrosion resistant material (e.g., stainless steel, nickel alloy, titanium, or zirconium). Due to the nature of this process, producible geometries are very limited. They must be simple. Typical geometries produced include plates, tubing and tubesheets.

1.5.2 Advantages and disadvantages

Explosion welding can produce a bond between two metals that cannot necessarily be welded by conventional means. The process does not melt either metal, instead plasticizing the surfaces of both metals, causing them to come into intimate contact sufficient to create a weld. This is a similar principle to other non-fusion welding techniques, such as friction welding.

Large areas can be bonded extremely quickly and the weld itself is very clean, due to the fact that the surface material of both metals is violently expelled during the reaction.

A disadvantage of this method is that extensive knowledge of explosives is needed before the procedure may be attempted safely. Regulations for the use of high explosives may require special licensing.

1.6   Inertial perforation models

Analytical models, although limited in scope, are quite useful for developing an appreciation for the dominant physical phenomena occurring in a given impact situation and for sorting experimental data.

They may even be useful in making predictions, provided care is taken not to violate the simplifying assumptions introduced in their derivation or exceed the data base from which their empirical constants are derived. If a complete solution to impact situation is necessary, recourse must be made to numerical simulation. This is especially true for oblique impacts or situations where a three-dimensional stress state is dominant for there are virtually no models which can deal with such complexity.

Two and three-dimensional computer codes obviate the need for various simplifications and are capable of treating complex geometries and loading states. However, their accuracy and utility is limited by the material descriptions embodied in their constitutive equations. Excellent results have been obtained for situations where material behaviour is well understood and characterized [6].

Current interest centres on three dimensional simulations. The range of problems addressed is fairly wide, including computations in the hypervelocity regime in order to determine structural configurations capable of protecting structures against impacts and study of the erosion and fracture of punches or penetrators. The bulk of the effort has been on the military problems, namely the penetration and perforation of solids and structures subjected to kinetic energy missile and shaped charge attack as well as the reverse problem of the design of armours against such threats. In geophysics, computations complement study of materials under very high pressures and provide historical details for formation of craters produced by meteor impact [7]. Industrial problems addressable computationally include explosive forming, explosive welding, shock synthesis of materials, mining, and massive earth removal.

As said above, in the last years, many models were created to predict the effect on an impact. Surely the main analytical model of the perforation of metals, describing the strength properties of metallic sheets, is to Johnson and Cook 1983 [8]. It only describe the sheet fracture.

1.6.1   Johnson-Cook material model

Several authors used the J-C model [8], or its modified formulations, in order to investigate and describe problems such as ballistic impacts or, more in general, problems in which the strain-rate component was relevant.

The J-C model is the simplest model able to predict the mechanical behaviour of the materials under different loading conditions. Besides, as mentioned before, it is one of the most used material models, so it is implemented in many FEM codes and it is quite easy to find in literature the values of J-C parameters for different materials.

It gives the following relation for the flow stress σ_{yield} on the target surface:

$$\sigma_{yield} = [A + B(\overline{\varepsilon^p})^n][1 + C \, ln(\dot{\varepsilon}^*)][1 + (T^*)^m] \tag{1.41}$$

Where:

- A is the elastic limit strength;
- B and n are the work hardening parameters and influence the slope of the flow stress in the plastic domain. The parameter n usually assumes values between 0 (for perfectly plastic model) and 1 (for a piecewise linear model);
- $\overline{\varepsilon^p}$ is the effective plastic strain;
- $\dot{\varepsilon}^*$ is the nondimensional strain rate: ratio of the effective plastic strain rate $\overline{\dot{\varepsilon}^p}$ to the reference strain rate $\dot{\varepsilon}^0$ (usually equal to 1):

$$\dot{\varepsilon}^* = \frac{\overline{\dot{\varepsilon}^p}}{\dot{\varepsilon}^0} \tag{1.42}$$

  where $\dot{\varepsilon}_0$ is the reference strain rate $\dot{\varepsilon}^0$ (usually equal to 1);

- C expresses the strain-rate sensitivity coefficients;
- T^* is the nondimensional temperature:

$$T^* = \frac{T - T_{room}}{T_{melt} - T_{room}} \tag{1.43}$$

  where:

T is the current temperature;

Troom is the ambient temperature;

Tmelt is the melt temperature.

- m is thermal softening coefficient. It describes the thermal effects: in this condition, the material loses its shear strength and starts to behave like a fluid. The thermal parameter m determines the concavity of the temperature function: if m < 1 the function is convex, if m > 1 it is concave and if m = 1 the temperature influence is linear.

Adiabatic conditions are assumed such that all internal plastic work is converted into temperature change, i.e.:

$$\Delta T = \frac{\overline{\sigma \varepsilon^p}}{\rho C_V} \tag{1.44}$$

where

$\bar{\sigma}$ is the effective stress;

ρ is the mass density;

C_V is the constant volume specific heat.

The effective plastic strain $\overline{\varepsilon^p}$ is defined by:

$$\overline{\varepsilon^p} = \int_0^t d\overline{\varepsilon^p} \tag{1.45}$$

where the incremental plastic strain $d\overline{\varepsilon^p}$ is determined from the incremental plastic strain tensor $d\varepsilon_{ij}$, such that:

$$d\overline{\varepsilon^p} = \sqrt{\frac{2d\varepsilon_{ij}d\varepsilon_{ij}}{3}} \tag{1.46}$$

The effective stress $\bar{\sigma}$ is defined by:

$$\bar{\sigma} = \sqrt{\frac{3\sigma_{ij}\sigma_{ij}}{2}} \tag{1.47}$$

1.6.2   Johnson-Cook failure model

Failure accumulation in the J-C model does not directly degrade the yield surface. The model, more fully described in reference [9], defines the strain at fracture as:

$$\varepsilon_{failure} = \left[D_1 + D_2^{D_3\sigma^*}\right]\left[1 + D_4\ln(\dot{\varepsilon^*})\right]\left[1 + D_5 T^*\right] \qquad (1.48)$$

Where:

$D_1 \ldots D_5$ are constants;

σ^* is the ratio of the pressure to the effective stress, i.e.:

$$\sigma^* = \frac{pressure}{\bar{\sigma}} \qquad (1.49)$$

Fracture occurs in the Johnson-Cook model when the damage parameter D exceeds 1. The evolution of D is given by the accumulated incremental effective plastic strains divided by the current strain at fracture:

$$D = \sum \frac{\Delta\overline{\varepsilon^p}}{\varepsilon_{failure}} \qquad (1.50)$$

Where:

$\Delta\overline{\varepsilon^p}$ is the increment of equivalent plastic strain which occurs during an integration cycle;

$\varepsilon_{failure}$ is the equivalent strain to fracture.

1.7   Elements of internal ballistics

Internal ballistics or interior ballistics is the study of the propulsion of a un-powered projectile.

In guns, internal ballistics covers the time from the propellant's ignition until the projectile exits the muzzle. The knowledge of elements of internal ballistics was important, in our study, to adjust the impact velocity.

The internal ballistics is generally divided into 3 parts:
    a. Lock time, the time from sear release until the primer is struck;
    b. Ignition time, the time from when the primer is struck until the projectile starts to move;

c.   <u>Barrel time</u>, the time from when the projectile starts to move until it exits the barrel. Although the lock time for us has not great interest, the consistency of the ignition and barrel times affect and relate to the muzzle velocity (our desired outcome).
There are many processes that are significant.

The source of energy is the burning propellant. It generates hot gases that raise the chamber pressure. That pressure pushes on the base of the projectile, and causes the projectile to accelerate. The chamber pressure depends on many factors of which the most important are:

–   the amount of propellant that has burned;

–   the temperature of the gases;

–   the volume of the chamber.

The burn rate of the propellant depends not only on the chemical make up, but also on the shape of the propellant grains.
The temperature depends not only on the energy released, but also the heat lost to the sides of the barrel and chamber.
The volume of the chamber is continuously changing: as the propellant burns, there is more volume for the gas to occupy. As the projectile travels down the barrel, the volume behind the projectile also increases.
There are still other effects, some energy is lost in deforming the projectile and causing it to spin, there are also frictional losses between the projectile and the barrel, the projectile, as it travels down the barrel, compresses the air in front of it.

These processes affect the gun design. The breech and the barrel must resist the high-pressure gases without damage. Although the pressure initially rises to a high value, the pressure starts dropping when the projectile has travelled some distance down the barrel. Consequently, the muzzle end of the barrel does not need to be as strong as the chamber end.

In the following figure we can see the gas pressure inside a barrel as a function of the instantaneous volume measured between breech plug and projectile, and the velocity of the projectile:
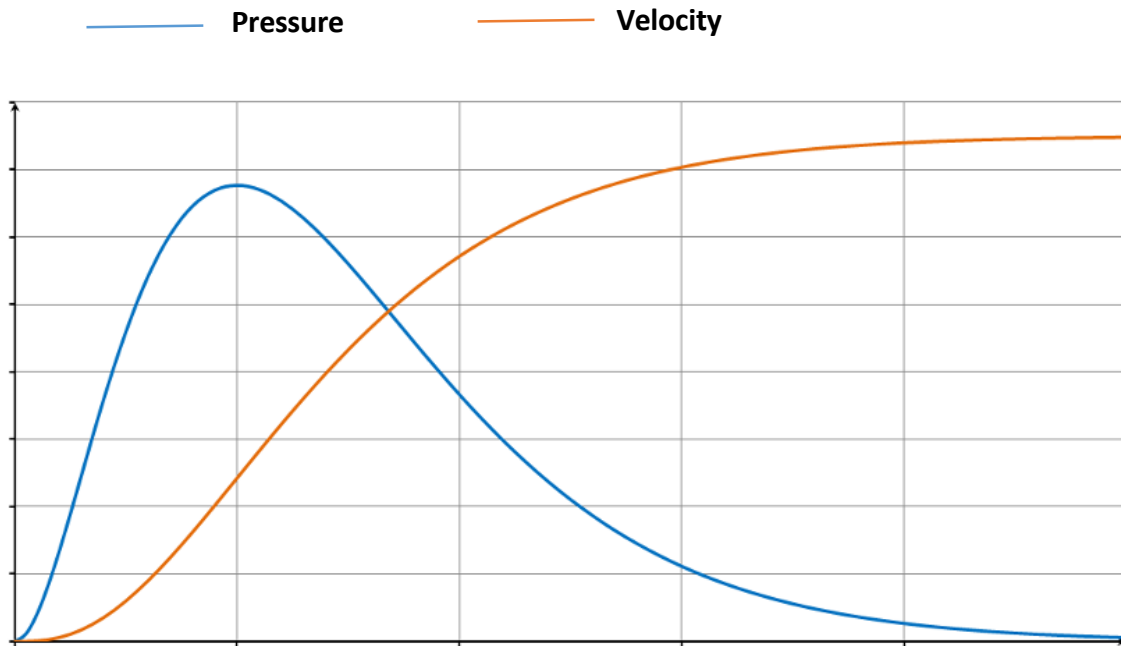
Figure 25: Pressure and velocity in barrel

Propellants used now are organic deflagrating powders and they can be divided into the following categories:

- single-base propellants: nitrocellulose;
- double-base propellants: nitrocellulose and nitroglycerin;
- three-base propellants; nitrocellulose, nitroglycerin and nitroguanidine.

Their composition allows to maintain a certain stability of behaviour that must be about constant regardless of environmental conditions and the state of preservation of the material.

In any case, it is important to understand that, in general, increasing the loading powder and using the same bullet, the muzzle velocity increase.
It is a quick way to adjust the impact velocity on the target.

1.8 Elements of external ballistics

External ballistics or exterior ballistics is the part of ballistics that deals with the behaviour of a projectile in flight. The projectile may be powered or un-powered (in our case we consider only un-powered or inertial projectiles), guided or unguided, spin or fin stabilized, flying through an atmosphere or in the vacuum of space, but most certainly flying under the influence of a gravitational field.

Gun-launched projectiles may be unpowered, deriving all their velocity from the propellant's ignition until the projectile exits the gun barrel (like in our tests). However, exterior ballistics analysis also deals with the trajectories of rocket assisted gun-launched projectiles and gun launched rockets. External ballistics is also concerned with the free-flight of other projectiles such as balls, arrows, etc.

1.8.1 Forces acting on the projectile

When in flight, the main or major forces acting on the projectile are **gravity** (Fg), **drag** (Fd), and if present, **wind** (Fw).

In small arms external ballistics applications, gravity imparts a downward acceleration on the projectile, causing it to drop from the line of sight. Drag, or the air resistance, decelerates the projectile with a force proportional to the square of the velocity. Wind makes the projectile deviate from its trajectory. During flight, gravity, drag, and wind have a major impact on the path of the projectile, and must be accounted for when predicting how the projectile will travel.

At extremely long ranges, artillery must fire projectiles along trajectories that are not even approximately straight; they are closer to parabolic, although air resistance affects this. Extreme long range projectiles are subject to significantly deflections, depending on circumstances, from the line toward the target; and all external factors and long range factors must be taken into account when aiming.

In the case of ballistic missiles, the altitudes involved have a significant effect as well, with part of the flight taking place in a near-vacuum well above a rotating earth, steadily moving the target from where it was at launch time.

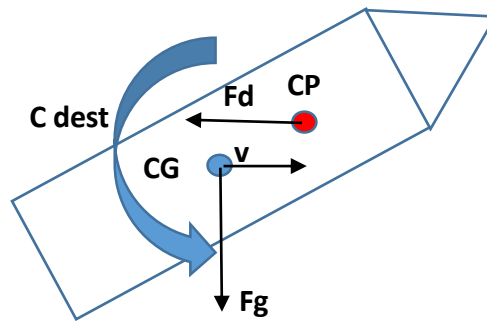In any case, the flying body is subject to the following forces:

Figure 26: Force system

We can see that, in this general situation, being the centre of pressure (CP) behind the centre of gravity (CG), without stabilizing strategies, the flying body is subjected to an overturning momentum (Cdest) that destabilize the trajectory.

In this condition, as we verified during our tests (next paragraph 2.2.1), the bullet will not arrive to the target in the right position.

1.8.1.1 *Stabilizing non-spherical projectiles during flight*

Two methods can be employed to stabilize non-spherical projectiles during flight:

- projectiles like arrows achieve stability by forcing their centre of pressure (CP) behind their center of gravity (CG) with tail surfaces. The CP behind the CG condition yields stable projectile flight, meaning the projectile will not overturn during flight through the atmosphere due to aerodynamic forces, because the flying body will be subjected to a stabilizing momentum (Cstab):
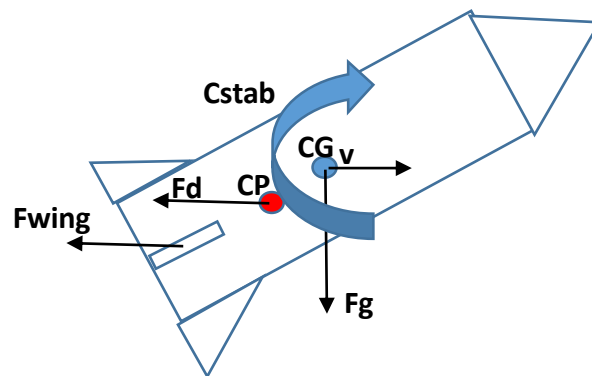
Figure 27: Arrows stabilization

- projectiles like small arms bullets and artillery shells must deal with their CP being in front of their CG, which destabilizes these projectiles during flight. To stabilize such projectiles the projectile is spun around its longitudinal (leading to trailing) axis. The spinning mass creates gyroscopic forces that keep the bullet's length axis resistant to the destabilizing overturning torque of the CP being in front of the CG.
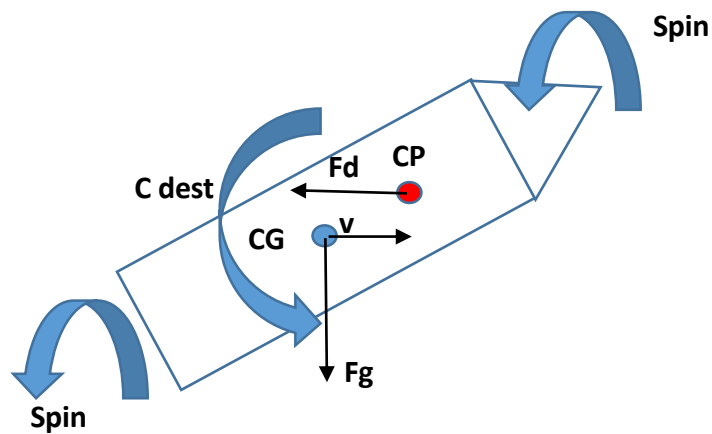
Figure 28: Spin stabilization

1.9   Inertial perforation problems – materials in use

The most efficient penetrators are made from either tungsten alloys, depleted uranium or cemented tungsten carbide, but alloy steel penetrators are also commonly used, because they are less expensive and less polluting, even if they are much less efficient.

In this paragraph we illustrate the characteristics, advantages and disadvantages that have the materials used for this scope.

1.9.1   Tungsten heavy alloys

Tungsten heavy alloys (WHAs) are composite materials made by liquid phase sintering, whereby tungsten powder is bound by a lower melting metal matrix, which contains most alloying elements.
It shows a typical microstructure where BCC tungsten particles (30–40 μm in diameter) are embedded in a FCC W–Ni–Fe solid solution matrix. Generally, liquid-phase sintered WHAs are fabricated by blending raw powders of tungsten, nickel and iron and sintering at a temperature above 1460°C in a hydrogen atmosphere.

Due to their combination of high density, strength and ductility, WHAs are used as kinetic energy penetrators (Figure 29), counterweights, radiation shields, vibration damping devices, and electrical contacts.

Figure 29: WHA punch

Penetration capabilities are and are related to the adiabatic shear deformation resulting in the self-sharpening behavior of kinetic energy penetrators [10].

1.9.1.1 Limitations for use of tungsten heavy alloys

Tungsten, in normal conditions, is not classified as particularly dangerous for human health but the inhalation of the tungsten heavy metal dust, generated by the impact, could determine health breathing problems [11], especially in the shooting ranges used for training and material tests. For this reason, various researches are underway to develop alternative tungsten alloys [12].

In any case, the main problems concerning the use of WHA for penetration or perforation are its high cost and its slow degradation, due to its high corrosion resistance.

1.9.2 Depleted Uranium

Depleted uranium (DU) is uranium with a lower content of the fissile isotope U-235 than natural uranium (Natural uranium contains about 0.72% of its fissile isotope U-235, while the DU used by the U.S. Department of Defense contain 0.3% U-235 or less).
It is a by-product of the process of enrichment of natural uranium and is classified as a chemical toxic and as a radioactive waste [13].

The uses of DU take advantage of its very high density of 19.1 kg/dm^3.

Civilian uses include counterweights in aircraft, punching, radiation shielding in medical radiation therapy and industrial radiography equipment, and containers for transporting radioactive materials. Military uses include armour plating and armour-piercing projectiles (Figure 30).

Figure 30: DU piercing

Most depleted uranium arises as a by-product of the production of enriched uranium for use as fuel in nuclear reactors.

The use of DU in ammunitions is controversial because of concerns about potential long-term health effects [13].
It is only weakly radioactive because of its long radioactive half-life (4.468 billion years for U-238 and 700 million years for U-235).

The actual level of acute and chronic toxicity of DU is also controversial. Several studies using cultured cells and laboratory rodents suggest the possibility of leukemogenic, genetic, reproductive, and neurological effects from chronic exposure [14].

DU was preferred to WHA, for kinetic energy penetrators, for its ballistic efficiency and pyrophoricity [15]. In both materials, the main deformation and failure mechanism responsible for penetrator erosion is adiabatic shear banding, but DU is more efficient that WHA because it forms adiabatic shear bands more easily, thus keeping a sharper penetrator tip [16].

On impact the DU ignites, and part of the penetrator rod is eroded forming oxidized dust. Generally more than 50% of the dust particles have inhalable size and remain airborne for hours; moreover some are water soluble. The surface contamination initially involves an area of tens of meters, and can then spread due to wind and water streams. The DU dust can be

inhaled by people, including friends and civilians, immediately after the impact, causing long-term chemical-toxicological health risks, the target organ being the kidney.

Despite its favourable properties for kinetic penetrators, the use of DU has become controversial because of the above described actual and possible environmental and health dangers, which have been highlighted by its extensive uses in some recent conflicts, leading to a precautionary approach to its use or even its banishment in inertial applications.

1.9.2.1 Legal status in weapons

Many international organizations examined the legal status of DU in weapons but, at moment, there is no specific treaty ban on the use of DU projectiles.

There is a developing scientific debate and concern expressed regarding the impact of the use of such projectiles and it is possible that, in future, there will be a consensus view in international legal circles that use of such projectiles violate general principles of the law applicable to use of weapons in armed conflict.

No such consensus exists at present.

In the last few years, a number of academics specializing in international humanitarian law and many non-governmental organizations have questioned the legality of the continued use of depleted uranium weapons, highlighting that the effects may breach the principle of distinction (between civilians and military personnel) but, in any way, also for the boost of some countries, the use of depleted uranium is not prohibited by international law.

Being no specific international convention that prohibits its use, the judgment of the legality of weapons with Depleted Uranium is a function of the type of use.

Its use can be considered [17]:

- lawful in scientific and avionic and naval instrumentations technologies (for example, when used as a counterweight in naval and aerospace applications, when it is used for medical instruments, etc…);

- not lawful when the depleted uranium is used as a radiological weapon or chemical weapon;

- of dubious legality when the depleted uranium is used as armours of weapons systems or as armour-piercing ammunition (weapon that could cause persistent pain over time and severe damage, permanent or extended to natural environment).

1.9.3 Cemented tungsten carbides

Cemented tungsten carbide is a composite formed by liquid phase sintering, exhibiting dispersed tungsten carbide particles within a metallic matrix, usually made of cobalt (WC-Co).

For its good mechanical qualities, relatively high density (15,63 kg/dm^3 [11]) and exceptionally high hardness and compressive strength, it is used for cutting tools and as a penetrator material. The material is usually called cemented carbide, hardmetal or tungsten-carbide cobalt: it is a metal matrix composite where tungsten carbide particles are the aggregate and metallic cobalt serves as the matrix.

Sintered tungsten carbide cutting tools are very abrasion resistant and can also withstand higher temperatures than standard high speed steel tools. Carbide cutting surfaces are often used for machining through materials such as carbon steel or stainless steel, and in situations where other tools would wear away, such as high-quantity production runs (Figure 31).

Because carbide tools maintain a sharp cutting edge better than other tools, they generally produce a better finish on parts, and their temperature resistance allows faster machining.

Figure 31: WC-Co Punch

In particular, cemented tungsten carbide is often used in armour-piercing ammunition for its reasonable cost (cheaper than WHA), especially if DU is not available or is politically unacceptable.

1.9.3.1   Limitations for use of cemented tungsten carbides

The primary health risks associated with carbide relate to inhalation of the dust that could be generated in the impact [18], but the carcinogenic effect of cobalt must also be considered especially in shooting ranges [19].

This risk must be taken into consideration in closed environments (like mechanical workshops or the closed shooting ranges) or in areas where such perforation material is used intensely.

The cost of this material is particularly high and therefore this aspect also limits very much its use.

1.9.4   Alloy steels

In the last period, steel penetrators are much in use because they do not give problems of environmental sustainability or human health and then they are considered "green".

Alloy steels used as penetrators include some types of tool steels, such as high-speed tool steels [20] and cold-work tool steels, which can be heat treated to high hardness. Although their perforation efficiency is much lower compared to that of the above described materials, they are widely used for their low cost and for their fast degradation in the environment into non-polluting and non-hazardous oxides.

The dynamic behaviour of alloy steel penetrators involves their mechanical properties (like for exemple their hardness [21]) their deformation or fragmentation behaviour [22]; the latter increases with both armour thickness and impact angle.

This material is also widely used for punching both in woodworking and in steel working (figure 32):

Figure 32: Steel Punches

1.10 Aim of the study

The deformation and fracture behaviour of DU and WHA penetrators have been studied in great detail, and the importance of the microscopic deformation mechanisms, such as adiabatic shear banding, for the ballistic efficiency, have been proven [16].

On the contrary, even if hard steel penetrators are commonly used, little has been published in the open literature about the relationship between their deformation and fracture behaviour, either microscopic or macroscopic, and their ballistic efficiency.

This lack seems very strange, considering that the international community is paying much attention to issues related to environment, human health and economic saving.

Therefore, in this work, the impact deformation and fracture behaviour of armour-piercing penetrators fabricated with three tool steels, and their resultant perforation efficiency, are investigated, both to better understand the optimal mechanical properties of armour piercing materials, and to describe the fracture mechanics of the tested materials.

Moreover, the results of the three alloy steels are compared with those achieved by plain medium carbon steel and by cemented tungsten carbide.

2 Chapter II – Materials and methods

2.1 Piercing mode

The piercing mode used for the tests was ballistics because it ensures a practical way to vary or adapt all physical parameters and, above all, to measure them with simple equipment.

As we have see in the paragrafh 1.8, we adjusted the speed of the bullet by varying manually the amount of powder load. It was a very dangerous operation, performed by an experienced technical worker.

In this case, we can be sure that all impact phenomena that we performed were exclusively inertial.

2.2 Bullets and target design

About penetrator geometry, although we know how important it is for ballistic performance [23], we have chosen to follow the geometry of the commercial penetrators in WC-Co because we could make a comparison.

The penetrators (Figure 33) were mounted into a case fabricated with free-cutting brass (grade EN CuZn39Pb3, approximately equivalent to UNS C38500), which was purposefully designed (Figure 34).

Shorter tool steel penetrators, backed by sintered Cu-W rods (consisting of 25% Cu and 75% W, with density 15 kg/m3 and low hardness - Figure 33b) and mounted in the same brass case, were also used, to increase the overall bullet mass. The penetrator (as well as the back rod when used) and the case were mounted with a nominal interference of 0.01 mm (Figures 33 and 34).
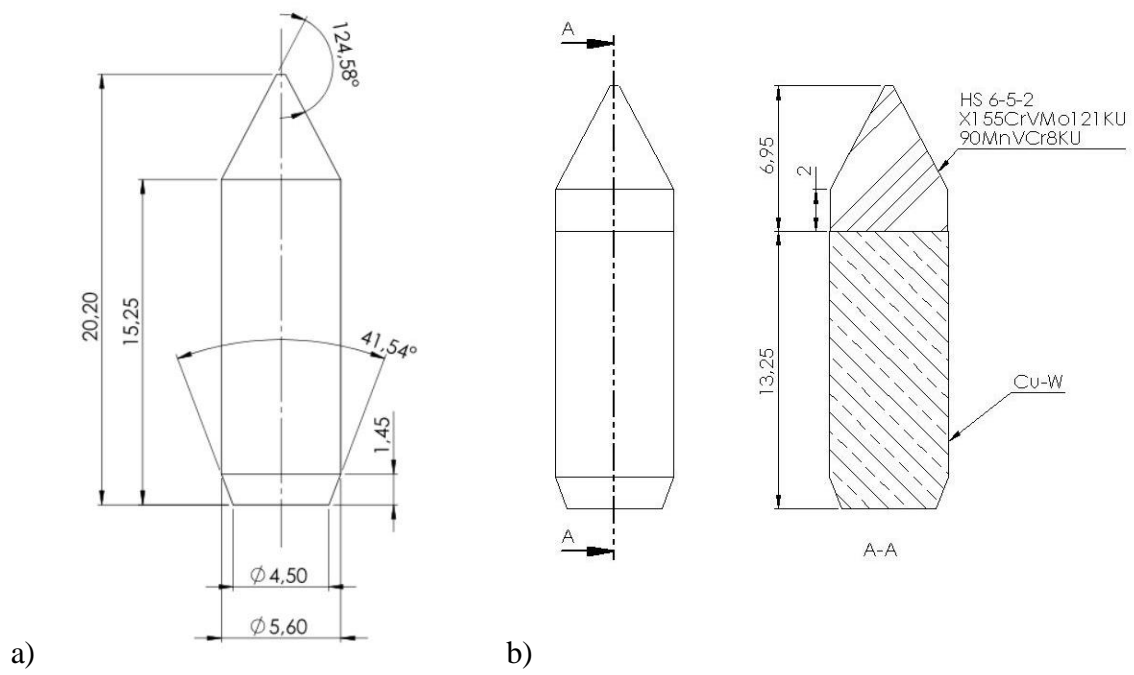
Figure 33: Penetrator (a) and modified penetrator with Cu-W back rod (b)
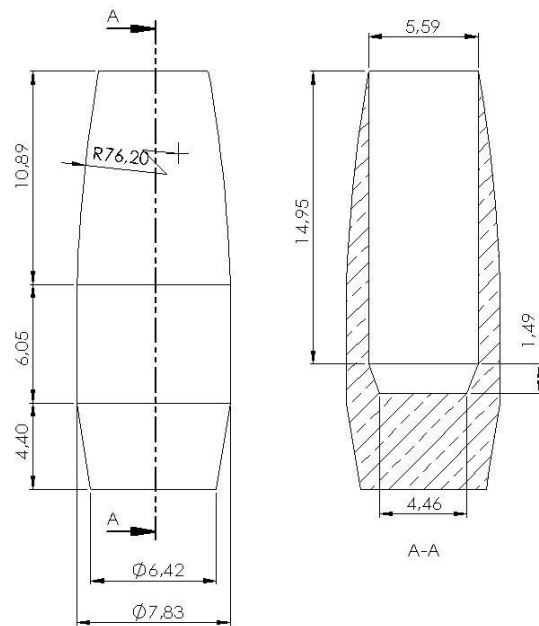
Figure 34: Brass case

All bullets exhibit a widely used gauge, corresponding to the civilian standard cal. .308 Winchester and to the military standard 7.62 NATO (7,62x51 mm) and they result like the following sample (Figure 35).

Figure 35: Test bullet

The target was a 6 mm thick, 450 mm wide square low alloy steel plate, hardened to $51 \div 52$ HRC1 (Figure 36).

Figure 36: Target with target support and collecting cotton sheets

---

[1] The steel plates were manufactured from the steelworks SSAB AB, Stockholm, Sweden, under the trade name HARDOX 500.

2.2.1 Project projectile and external ballistics

At the beginning of the study, we did not want to use a heavy brass case like that described above, so we tried different configurations in which the penetrator was placed in a plastic case (Figure 37).

a   b

c

Figure 37: Plastic cases: commercial plastic sabot (a); test PVC case (b); test SLA case made by additive manufacturing

Despite this effort, the ballistic results obtained were not satisfactory because the bullets did not reach peak on the target, highlighting, in this way, their dynamic instability (Figure 38):

Figure 38: Penetrator pierce the plate with a lateral impact

This has shown us that our projectile was not properly stabilized because, probably, the plastic material of its case did not resist the forces that suffered in the interior ballistics tract.

For this reason, we could not avoid a metal case and we chose the configuration shown previously.

We also tried different geometries for the case:
– Rear case (geometry in Figure 34);
– Front case (Figures 37c and 39):

Figure 39: Front brass case

The instability tested with the plastic back cases was replied also with front cases and this confirmed us that there was a problem with material properties (as we can see in figure 37c, we tested also plastic front cases).

We have chosen to use the back case for the following two reasons:

- because it's an easier geometry to be implemented by CNC machines;
- because we preferred that the impact were made directly by the penetrator, without interposed material.

2.2.2 Kinetic energy

With the stabilization method used for the configuration that we have chosen, the kinetic energy involved in the phenomenon is the sum of translational kinetic energy (KE_T) and rotational kinetic energy (KE_S):

$$KE = KE_T + KE_S \tag{2.1}$$

but, as we will verify, the second contribute can be neglected because, considering the velocity in play (translational and angular), it has very marginal importance.

In fact, assuming to regularize the geometry of our projectile to that of a cylinder, we could write:

$$KE_T = \frac{1}{2}mv^2 \tag{2.2}$$

and

$$KE_S = \frac{1}{2}I\omega^2 \tag{2.3}$$

where:

$I = \frac{1}{2}mr^2$ = moment of inertia of the cylinder;

$\omega^2 = v\frac{2\pi}{P}$ = angular speed;

P = pitch of the barrel rifling: 0,3048 m (see paragraph 2.4).

Comparing the dimensions we can see that:

$$\frac{KE_T}{KE_S} = \frac{\frac{1}{2}mv^2}{\frac{1}{2}I\omega^2} = \frac{\frac{1}{2}mv^2}{\frac{1}{2}\frac{mr^2}{2}\omega^2} = \frac{\frac{1}{2}mv^2}{\frac{1}{2}\frac{mr^2}{2}v\frac{2\pi}{P}} = \frac{v}{r^2\frac{\pi}{P}} \tag{2.4}$$

with, in our case:

$v \approx 350 \div 900$ m/s;

$r^2\frac{\pi}{P} \approx 8 \cdot 10^{-5}$ m

the order of magnitude translational kinetic energy is much higher than the rotational kinetic energy. For this reason we can neglect its contribute.

2.3   Penetrator materials

The following penetrator materials were examined:

- C45 medium carbon steel (approximately equivalent to AISI 1045), heat treated to a final hardness of 23 HRC;
- 90MnVCr8KU cold work tool steel (AISI O2), heat treated to 57 HRC;
- X153CrMoV12 cold work tool steel (AISI D2), heat treated to 58 HRC;

- HS 6-5-2 high speed tool steel (AISI M2), heat treated to 49 HRC;
- WC-Co cemented tungsten carbide, with hardness 71 HRC.

The examined WC-Co penetrators are industrially produced and currently mounted into various ammunition, cal. 7,62x51 mm2; whereas the steel penetrators were purposefully fabricated with the same shape from commercial steel bars and then quenched and tempered. The chemical composition of the examined tool steels3 is given in Table 1, and their heat treatment schedule4 is given in Table 2.

After the heat treatment, the microstructure of both 90MnCrV8 and X153CrMoV12 cold work steels exhibits tempered martensite and retained austenite; whereas the HS 6-5-2 high-speed steel exhibits a tempered martensite matrix with dispersed spheroidal carbides (Figure 40).

Steel grade	C	Si	Mn	P	S	Cr	Mo	V	W
90MnCrV8	0.88	0.26	2.04	0.015	0.009	0.25	-	0.08	-
X153CrMoV12	1.52	0.3	0.27	0.023	0.009	11.38	0.73	0.74	-
HS 6-5-2	0.91	0.22	0.32	0.028	0.0003	3.99	4.86	1.78	5.92

Table 1 - Chemical composition of the examined tool steels, wt.%.

Steel grade	Austenitizing	Quenching	Tempering		
			1st	2nd	3rd
90MnCrV8	830 °C	Oil	270 °C / 1 h	-	-
X153CrMoV12	1100 °C	Nitrogen, 7 bar	550 °C / 1 h	550 °C / 1 h	550 °C / 1 h
HS 6-5-2	1200 °C	Nitrogen, 7 bar	620 °C / 1 h	620 °C / 1 h	620 °C / 1 h

Table 2 - Heat treatment schedule of the examined tool steels.

---

[2] The examined WC-Co penetrators were extracted from ammunition sold by Ruag Ammotec GMBH, Furth, Germany, and by Nammo AS, Raufoss, Norway.

[3] The steels and their heat elemental analysis were supplied by SACMA Acciai Speciali S.p.A, Torino, Italy.

[4] The heat treatment was performed by OMT Officine Meccaniche Torino S.p.A., Torino, Italy.
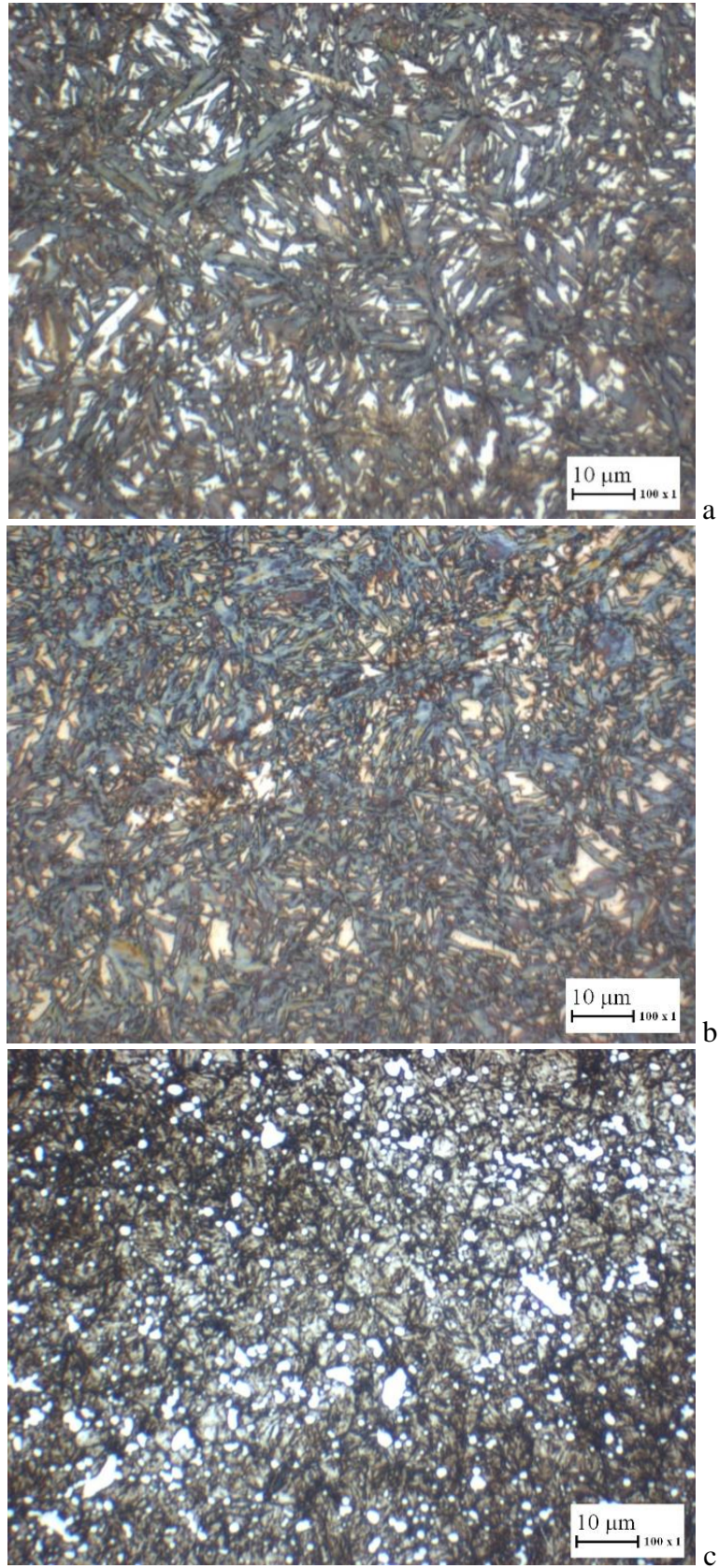
Figure 40: Microstructure of as-fabricated tool steel penetrators (cross section with Nital etching): 90MnVCr8KU (a), X153CrMoV12 (b) and HS 6-5-2 (c)

The following image (material examined by scanning electron microscopy) shows the structure of sintered Cu-W rods, used to increase the mass of the armor-piercing projectile (Figure 41):
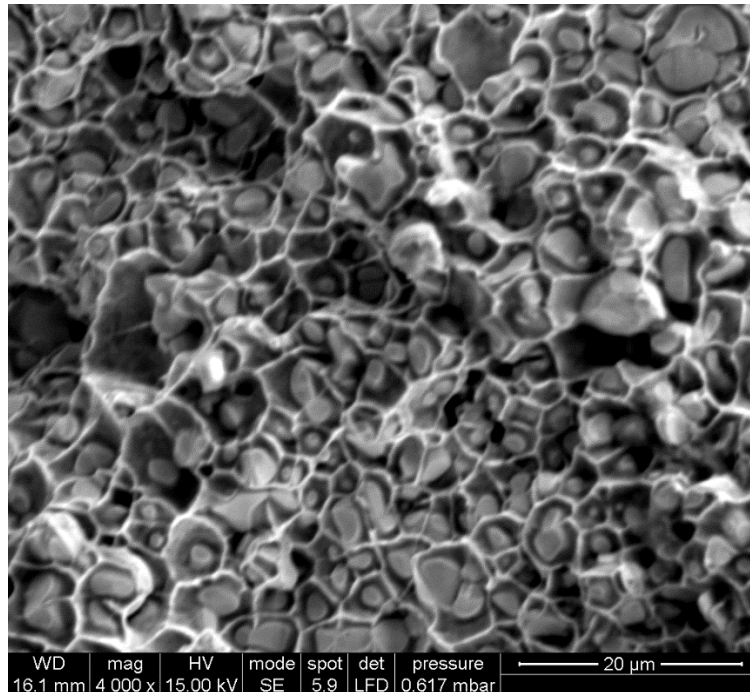
Figure 41: Microstructure of Cu-W rod

We can see easily that tungsten is embedded in a soft matrix of Copper.

2.4 Firing setup and procedure

The bullets were fired in an indoor shooting range, by using a 7.62 mm (bore diameter) barrel; the pitch of the barrel rifling was 304,8 mm (Figure 42).

Figure 42: Firing system

As shown in figure 43, the barrel rifling is nitrided to have a hardened bore surface:
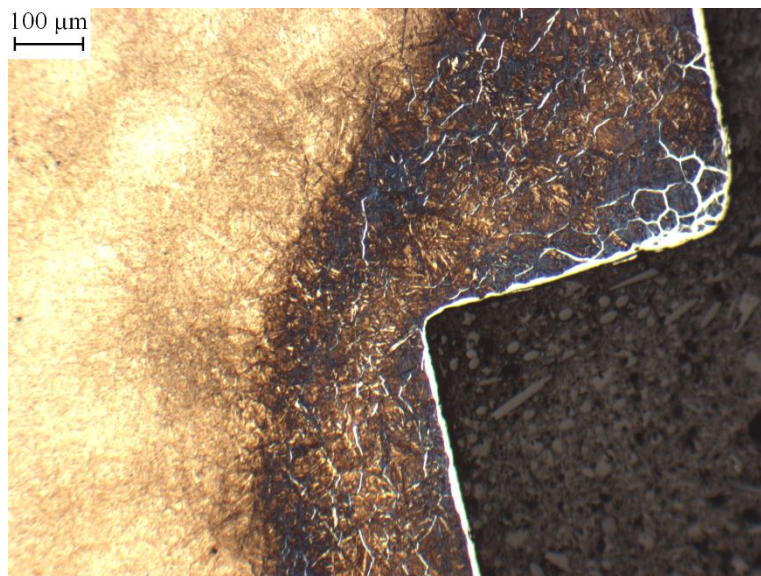
Figure 43: Nitrided barrel rifling

The bullet speed was measured by using a couple of light barriers, which were located at a distance of 0.2 and 1.2 m, respectively, from the barrel exit end (scheme in Figure 44). The loss of speed between the point of measure and the target was neglected.
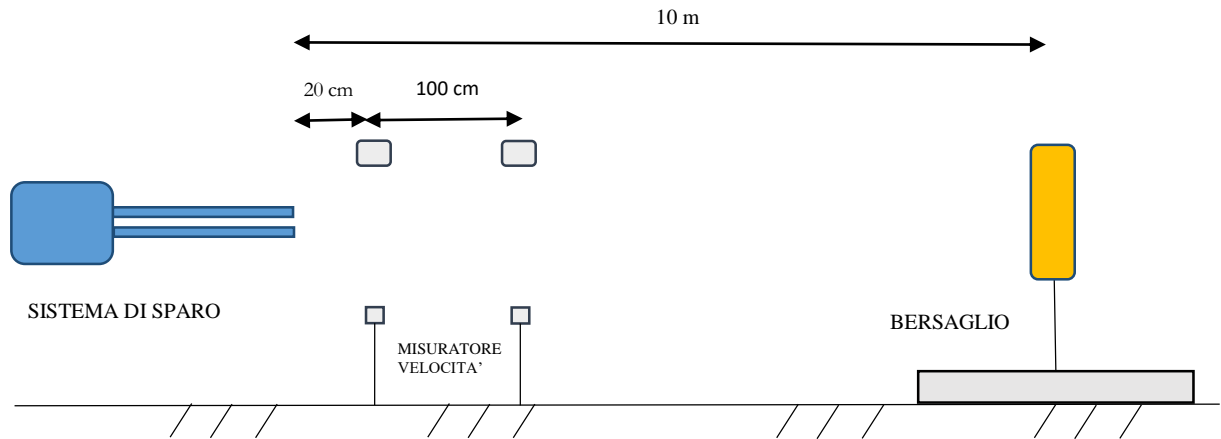
Figure 44: Configuration of test equipment

The target plate was 10 m away from the barrel exit end, and it was normal to the trajectory of the bullet within $\pm$ 3°, compliant to the standard STANAG 2920 [24].

In order to obtain repeatable and comparable results, the target, the barrel and the ammunition were held at a temperature of 20 °C $\pm$ 2 °C and at a relative humidity of 65% $\pm$ 5% for 24 hours before the ballistics test, and in the indoor shooting range the ambient temperature was 20 °C $\pm$ 5 °C and the relative humidity was 65% $\pm$ 10% (compliant to [24]).

For each type of bullet, a series of tests were carried out with different speeds, by manually adjusting the amount of gunpowder, in order to identify the V_{50} speed, which is defined as the bullet velocity which yields a 50% probability of perforation of a given target [24]. V_{50} was determined as the mean of three perforating and three non-perforating shots, all comprised in a speed range of 40 m/s or less [24]. The corresponding translational kinetic energy, here named KE_{50}, was calculated from V_{50} and from the bullet mass (the rotational kinetic energy was neglected).

The following picture (Figure 45) shows the target after a test session.

Figure 45: Target after a test session

After perforating shots, bullet and target fragments were collected for macroscopic, fractographic and metallographic analyses. The fragments were slowed and recovered behind the target by using cotton.

2.5   Repeatability of results

The efficiency of the firing procedure illustrated above was verified by repeating testes four times during one year.
In this way we wanted to observe if our test procedure gave us repeatable results.

The maximum tolerance that we found amounts to 2% of the measures listed in Table 3 (corresponding to tests carried out the day 14/01/2015).

3 Chapter III – Results and discussion

3.1 Perforation efficiency

The bullet mass, penetrator hardness, V_{50} speed and KE_{50} kinetic energy are reported in Table 3 below (speed dates of tests carried out the day 14/01/2015).

Penetrator type	Bullet mass [g]	Penetrator hardness [HRC]	V_{50} [m/s]	KE_{50} [J]	Perforating shots, speed [m/s]			Non perforating shots, speed [m/s]		
C45	7.50	23	828.0	2571	844	834	834	823	812	821
90MnCrV8	7.46	57	707.5	1867	717	708	708	701	704	707
90MnCrV8 with Cu-W back rod	9.65	57	757.2	2766	778	765	769	738	742	751
X153CrMoV12	7.40	58	672.3	1672	681	679	678	664	660	672
X153CrMoV12 with Cu-W back rod	9.65	58	738.6	2632	742	749	747	722	738	734
HS 6-5-2	7.56	49	661.5	1654	664	661	660	656	667	661
HS 6-5-2 with Cu-W back rod	9.69	49	710.2	2444	730	722	712	694	700	703
WC-Co	10.18	71	353.2	635	369	364	357	346	334	349

Table 3 - Bullet and penetrator properties and ballistic test results.

Since the target was always the same, V_{50} is a measure of the relative ballistic efficiency of the different bullets. The most efficient penetrator material of the examined set is the cemented tungsten carbide ($V_{50} = 353,2$ m/s) and the worst it the C45 steel grade (828 m/s). Among the examined steels, the most efficient is the HS 6-5-2 high speed steel (661,6 m/s). In general, the kinetic energy of a bullet in part is employed to deform and pierce the target, and in part is spent to deform the bullet itself. If the bullet hardness and yield strength increase, the energy spent for the bullet deformation decreases, thus the energy available for the target deformation and piercing increases, and the ballistic efficiency increases, i.e., V_{50} decreases [1-2].

The present results generally confirm the above rule, as highlighted in figure 46: the cemented tungsten carbide is both the hardest and the most efficient material, the C45 steel is the softest and least efficient, and the tool steels as a group exhibit intermediate hardness and efficiency.

However, the three tool steels are not fully consistent with the same rule; in particular, the high speed steel HS6-5-2 is the most efficient among them, in spite of its lower hardness.
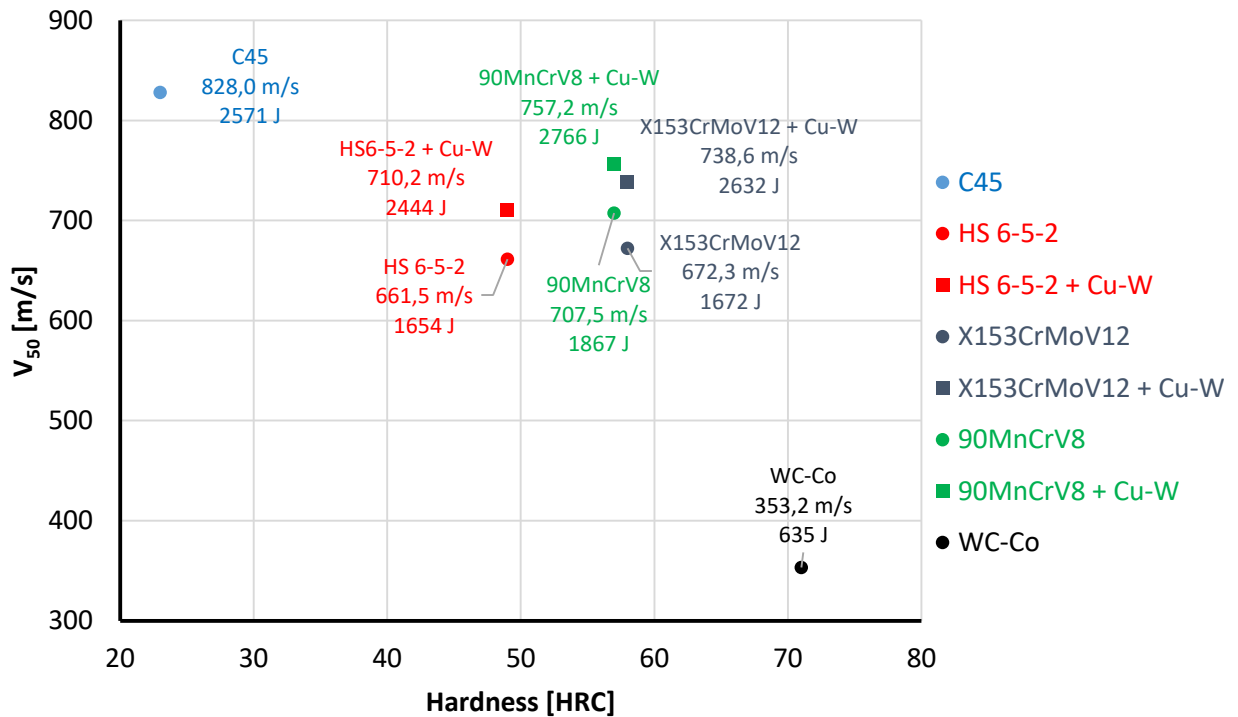
Figure 46: Ballistic efficiency (as measured by V₅₀ speed) vs. hardness, for the examined bullets

Moreover, by increasing the bullet mass with the heavy but soft Cu-W back-rod, while using a shorter penetrator of the same material, the efficiency of the tested steel penetrator bullets decreases (Table 3 and Figure 46). This loss of efficiency is probably caused by the energy loss due to the deformation of the Cu-W back rod, which is much softer than the examined steel grades, and thus is deformed much more extensively (Figure 47a). Therefore, in order to pierce the target, the bullets with the Cu-W back-rod must carry a much higher kinetic energy: KE_{50} increases by about 880 kJ, or 50 %, on average. Due to their higher mass, they can carry the same kinetic energy with a lower speed, but overall the former effect prevails, and V_{50} slightly increases (by 63 m/s, or 9%, on average).

It should be noted, however, that the present tests were not suitable to highlight the advantage of heavier bullets, because they were performed at short range (less than 10 m), and therefore the energy loss due to aerodynamic forces was negligible in all cases (heavier bullets carrying the same kinetic energy are slower, thus they undergo lower aerodynamic forces for the same shape, and ultimately lose less energy while flying the same distance).

3.2 Macroscopic analysis of fragments

The typical appearance of the full-lenght penetrators, and fragments thereof, which were recovered after perforating shots (with bullet speed close to V_{50}), is shown in Figure 47, for each examined penetrator material.

Most recovered cemented tungsten carbide penetrators were apparently intact, with no macroscopic deformation or fractures (Figure 47b). On the contrary, all recovered steel penetrators undergo the fracture and loss of their tip (Figures 46c to 47f); moreover, the softer C45 steel penetrators also undergo significant plastic deformation (Figure 47c).

The penetrator tip fracture occurs close to the same position in all cases, and can be due to a tensile stress wave generated when the compressive impact wave is reflected by a free boundary, as previously described in paragraph 1.4.3.

Moreover, all examined perforating shots formed a target fragment, or plug, with the shape of a cylinder with diameter close to the penetrator diameter, and length close to the target thickness (Figure 48).
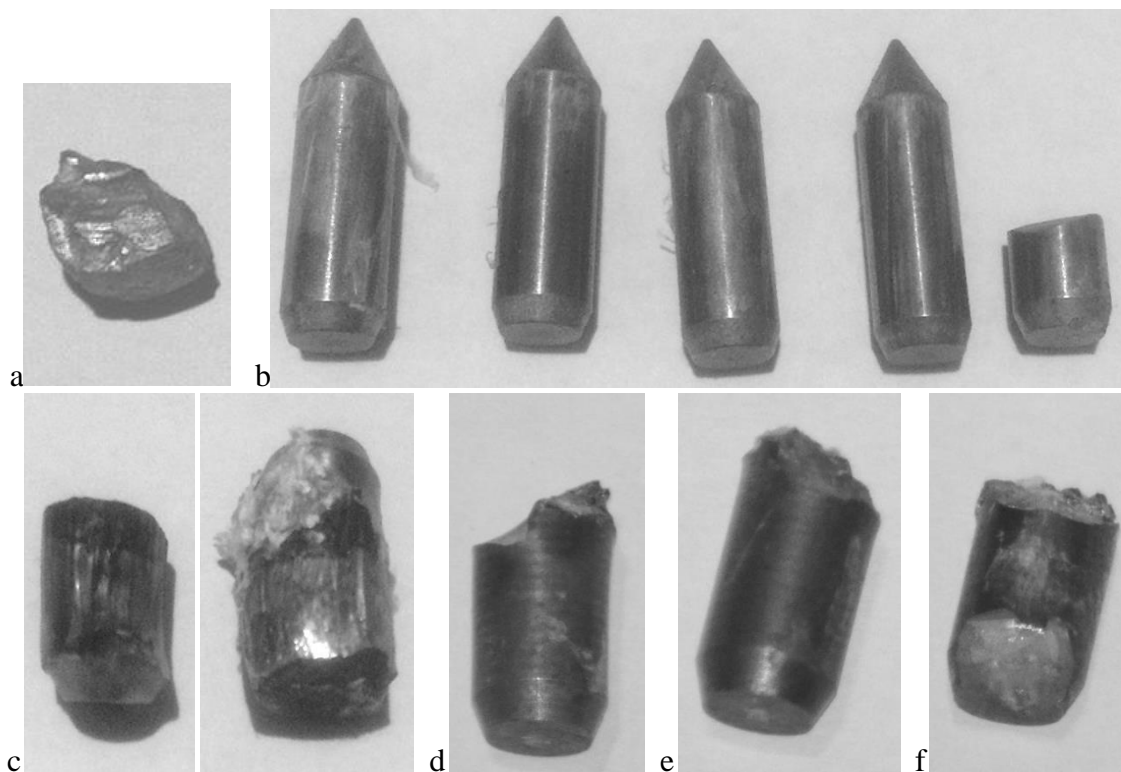
Figure 47: Bullet fragments recovered after perforating shots: Cu-W back-rod (a); cemented tungsten carbide penetrators (b); C45 (c), 90MnCrV8 (d), X153CrMoV12 (e), and HS6-5-2 (f) steel penetrators
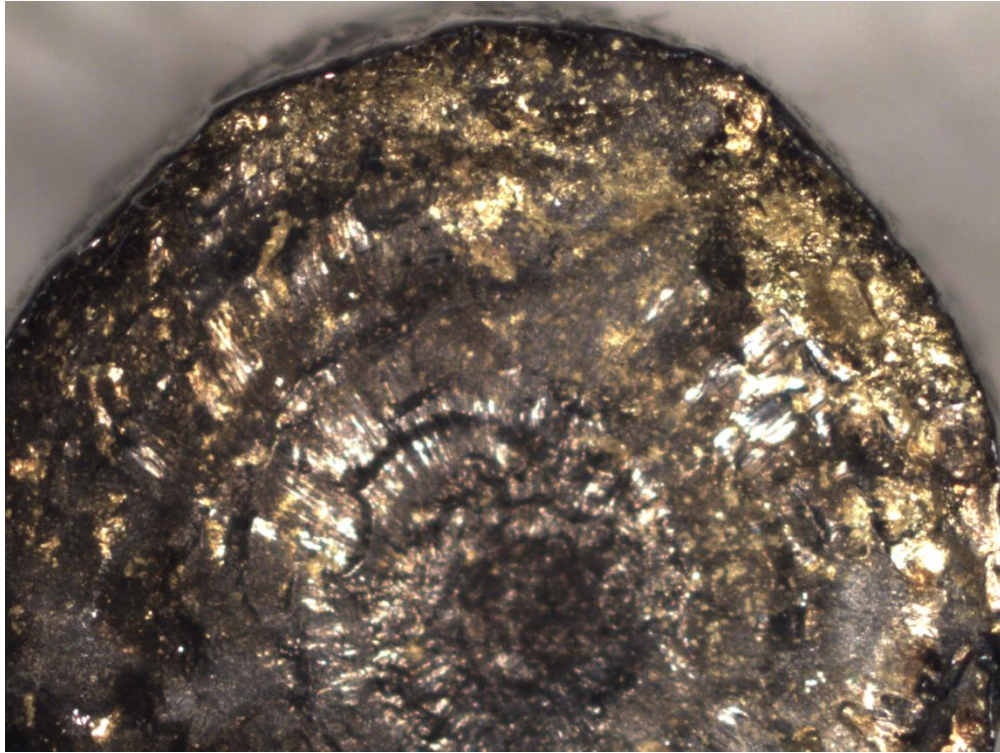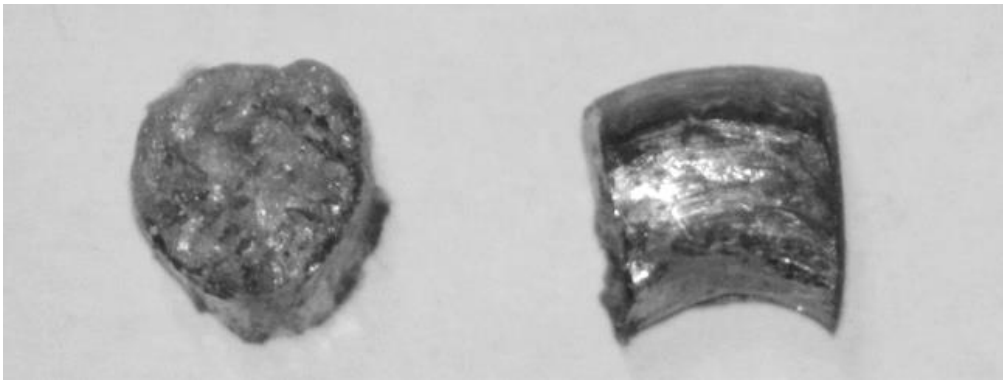
Figure 48: Target fragments, or plugs, formed by perforating shots

Careful examination showed that the broken penetrator tip was permanently joined to the plug, probably by explosion welding (Figure 49).
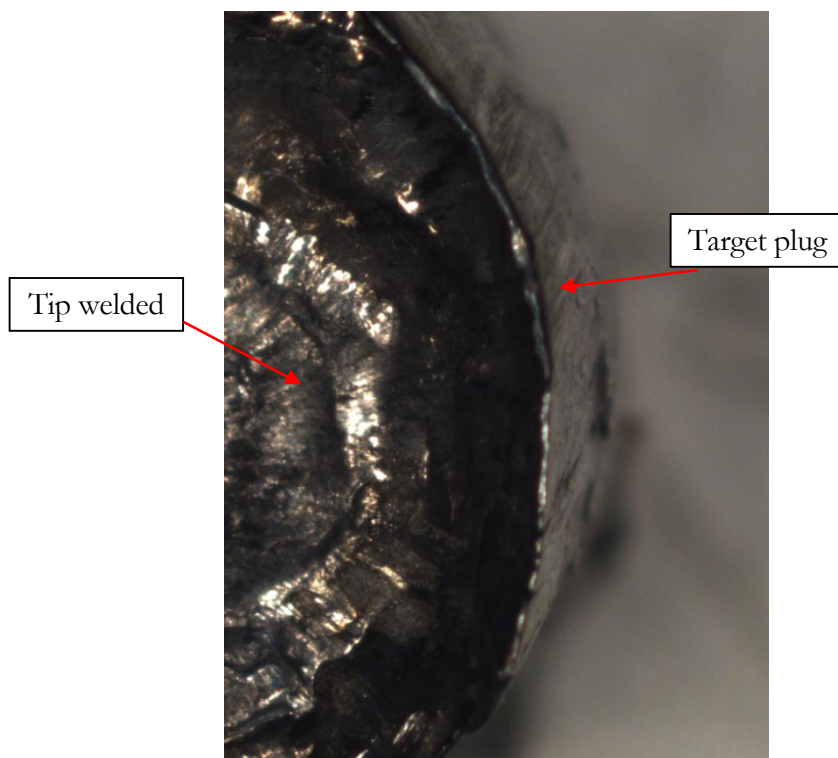
Figure 49: Tip welded to the target plug

Finally, in all cases a thin brass deposit was found on the target plate, forming a rim around the entry of the hole pierced by the penetrator, thus confirming that the brass case flew together with the penetrator, and parted from it on impact (Figure 50).

Figure 50: Brass rim around the holes of the target

3.3   Fractographic analysis of penetrator fragments

The fracture surfaces of representative tool steel penetrators, recovered after perforating shots, was examined by scanning electron microscopy (Figures 51 to 53).

In all cases, the fracture surface was formed mainly by adiabatic shear fracture; adiabatic shear planes are evident at low magnifications, and the shear direction can be deduced, at high magnification, on the basis of the orientation of the microscopic features on the shear planes. However, intergranular and ductile fracture features were also found in limited portions of the fracture surfaces, in particular in the 90MnCrV8 tool steel grade (Figure 53).
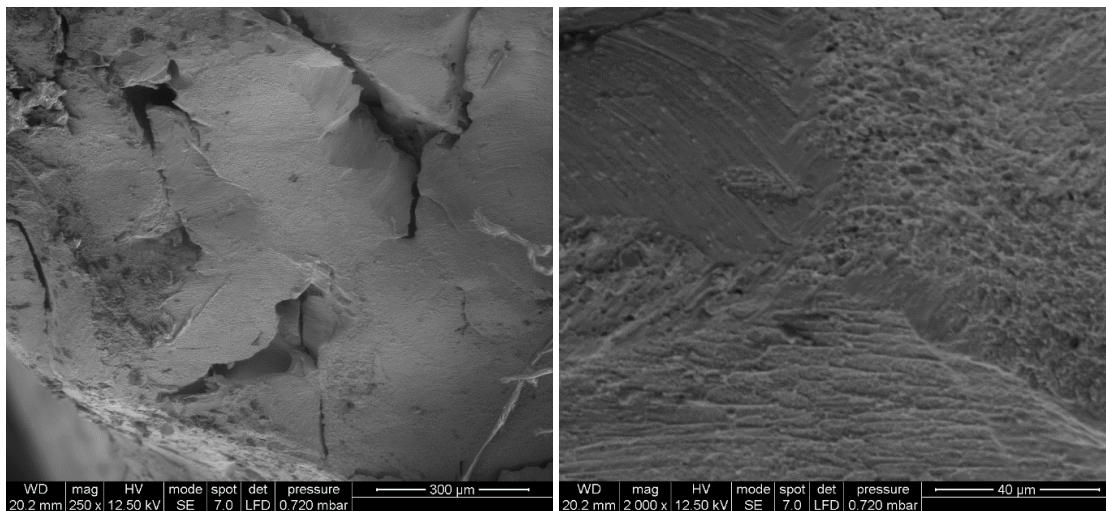
Figure 51: HS6-5-2 penetrator fractured in a perforating shot; increasing magnification
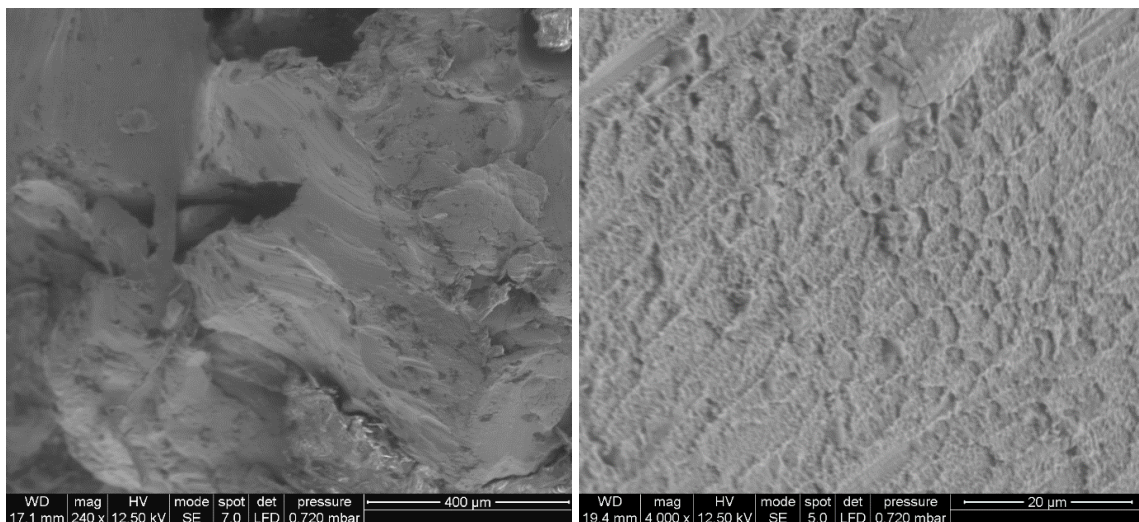
Figure 52: X153CrMoV12 penetrator fractured in a perforating shot; increasing magnification
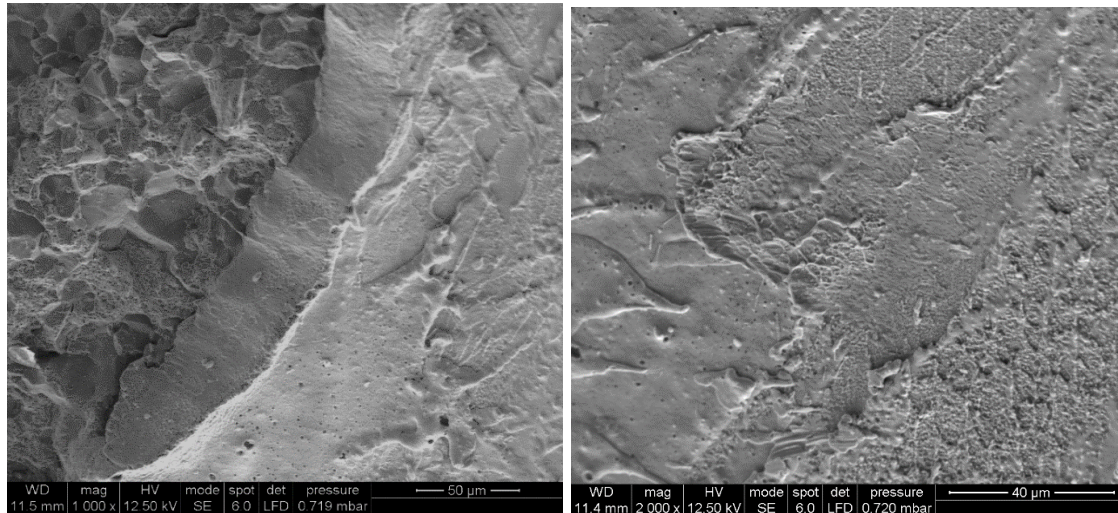
Figure 53: 90MnCrV8 penetrator fractured in a perforating shot; increasing magnification

3.4 Metallographic analysis of plugs

The above mentioned plugs, formed by penetrating shots with (full-length) tool steel penetrators, were mounted, polished and etched with Nital (3 vol. % nitric acid, ethanol), exposing a longitudinal metallographic plane.

In all cases, both the target plate material and the broken penetrator tip could be identified, and it was ascertained that the they had been welded in the impact, and that both showed adiabatic shear bands. Moreover, it was ascertained that both welding (between the target plate material and the penetrator tip) and fracture (of the penetrator tip) occurred on shear bands.

This is illustrated in more detail in Figures 54 to 56, in which the target plate material is on the right and the penetrator tip on the left. It is evident from these pictures that, while the overall phenomena are the same in the three cases, the amount of shear bands in the target plate material and in the three different penetrators is remarkably different; in particular, the HS6-5-2 tool steel grade (Figure 54) exhibits the smaller amount of shear bands in the penetrator tip (much less than the adjacent target plate material), the 90MnCrV8 grade (Figure 56) exhibits the larger amount of shear bands (much more than the target material), and the X153CrMoV12 (Figure 55) gives intermediate results.

The latter observations are consistent with the ballistic results, since they confirm that the tool steel grade which achieved the best ballistic efficiency (i.e., the HS6-5-2) also showed the least plastic deformation, and vice versa.

76
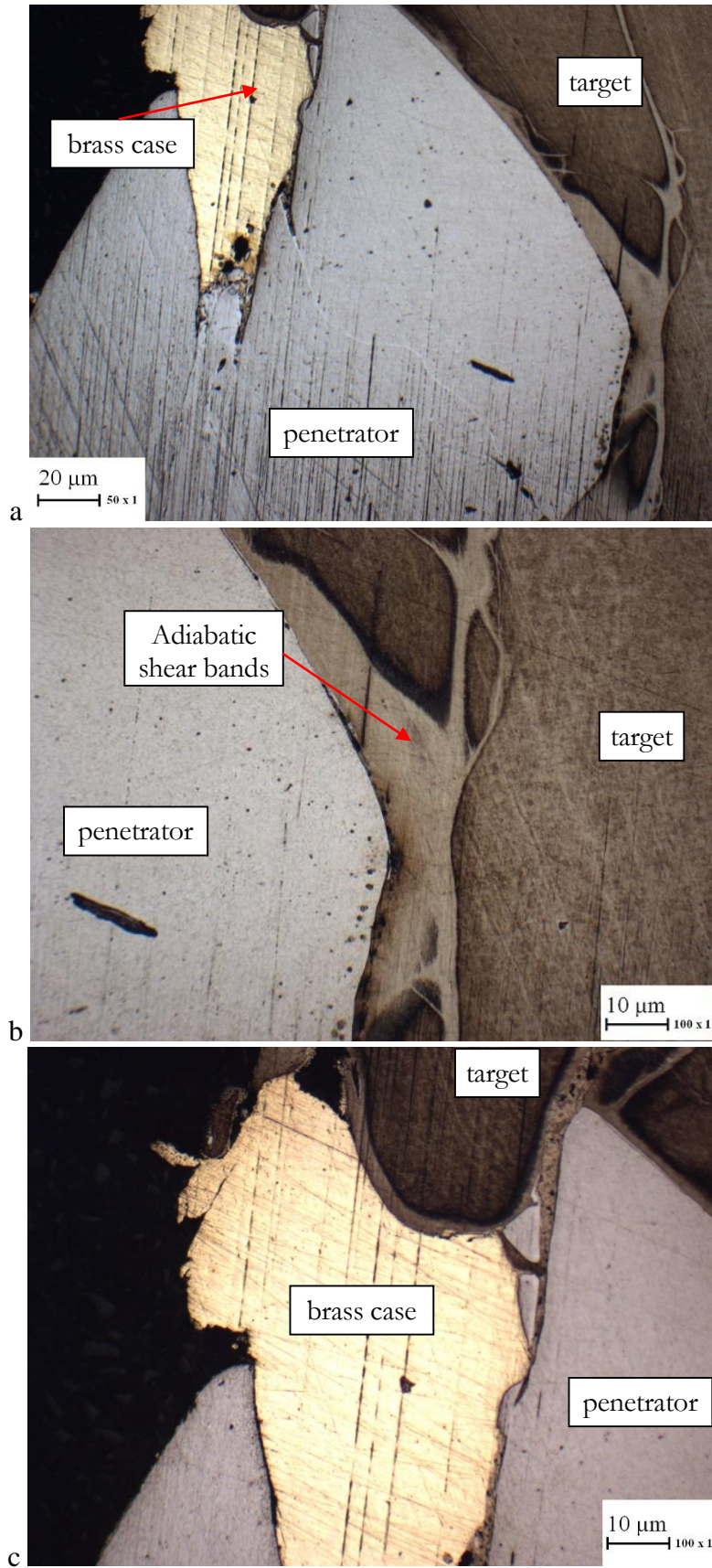
Figure 54: Etched longitudinal cross section of the plug formed by a HS6-5-2 tool steel penetrator
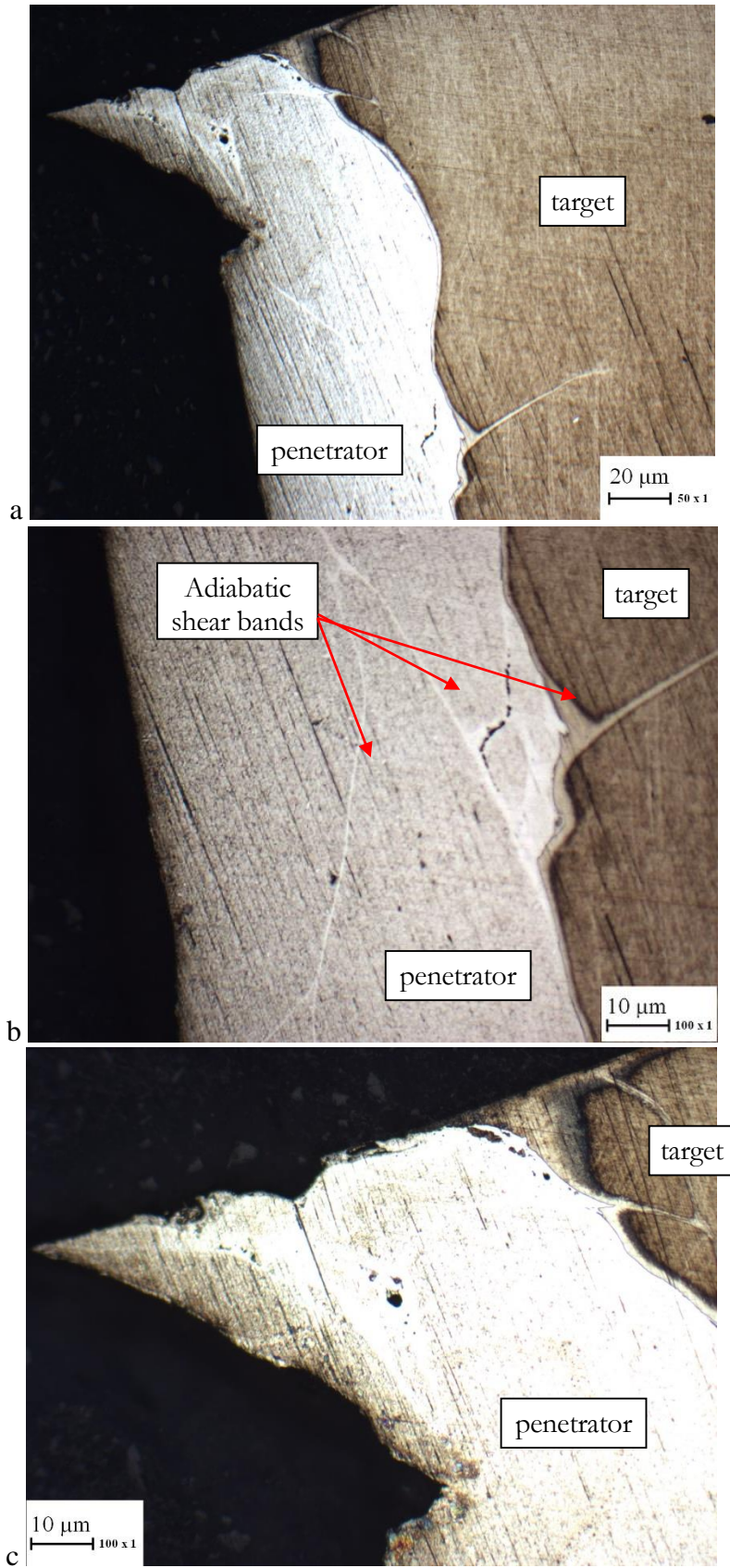
Figure 55: Etched longitudinal cross section of the plug formed by a X153CrMoV12 tool steel penetrator
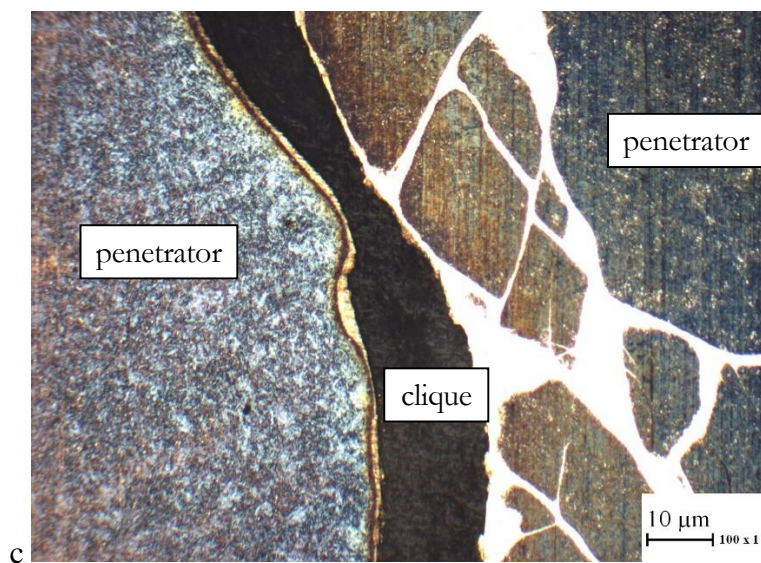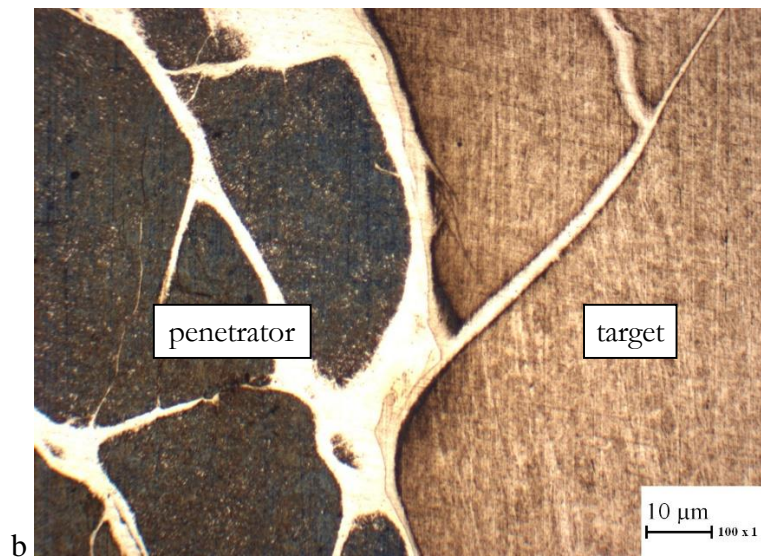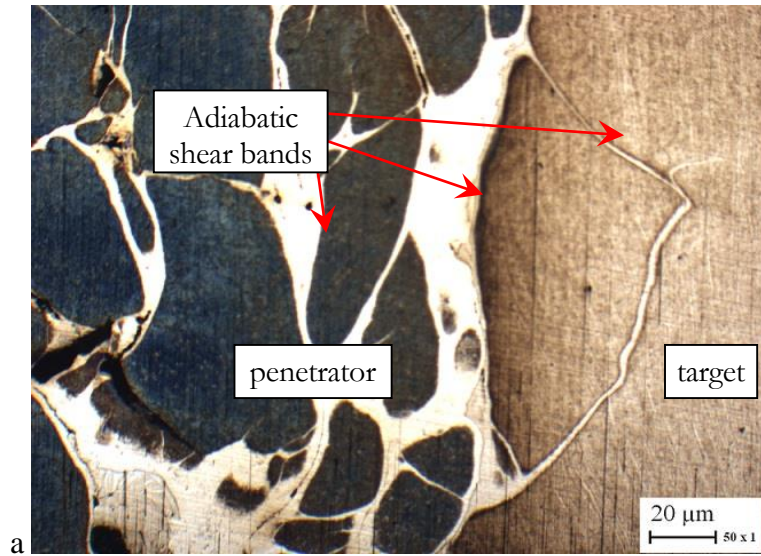
Figure 56: Etched longitudinal cross section of the plug formed by a 90MnCrV 8 tool steel penetrator

4 Chapter IV – Conclusions

4.1 Hardness and piercing efficiency

The efficiency of the examined armor-piercing penetrator materials, as measured by the V_{50} perforation speed against 6 mm thick hardened steel armor is, in general, directly correlated with their hardness. The cemented tungsten carbide is both the hardest and the most efficient material (hardness 71 HRC and $V_{50} = 353,2$ m/s), the C45 (or AISI 1045) steel is the softest and least efficient (23 HRC and $V_{50} = 828$ m/s), and the tool steels as a group exhibit intermediate hardness and efficiency (49 - 57 HRC and 661 - 707 m/s).

However, among the three tool steels, the high speed steel HS6-5-2 (or AISI M2) is the most efficient (661 m/s), even if it is the least hard (49 HRC), whereas the two cold work tool steels, 90MnVCr8KU and X153CrMoV12 (AISI O2 and D2) are very close between them (57 and 58 HRC, and 708 and 672 m/s, respectively).

Moreover, by increasing the bullet mass with a heavy but soft Cu-W back-rod, while using a shorter penetrator of the same material, the efficiency of the tested steel penetrator bullets decreases, probably due to the large energy loss due to the deformation of the Cu-W back rod.

Careful examination of recovered bullet fragments allows to describe qualitatively the impact events, and therefore to clarify the above ballistic efficiency results:

- in all cases, the brass case flies together with the penetrator, and parts from it on impact (Figures 50 and 57);
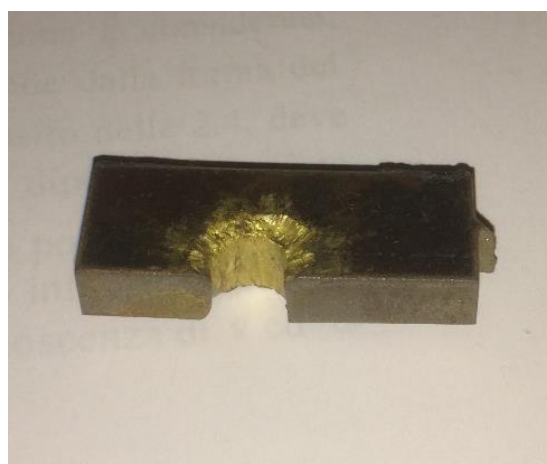
Figure 57: Brass rim on a section of a hole of the target

- in most cases, the cemented tungsten carbide penetrator can pierce the target without undergoing any macroscopic damage (Figure 47b);
- the softer materials (C45 steel penetrator and of the Cu-W back-rod) have undergone a very high deformation macroscopically (Figures 47a and 47c).

This shows us that, for the highest material (cemented tungsten carbide), thus nearly all kinetic energy can be used to deform and pierce the target, on the contrary, a large part of the kinetic energy of softer materials is spent in their own macroscopic plastic deformation.

The results described above are fairly predictable, in fact we can imagine that, with increasing hardness of the impacting material, increase its piercing capacity [25].
Also the speed steel piercing capacity is expected because its carbides increase the material toughness.

4.2 Fractures and welding

The steel penetrators generally undergo the fracture and loss of their tip.

It is a expected because, as described on paragraph 1.4, this tip fracture can be due to a tensile stress wave generated when the compressive impact wave is reflected by a free boundary (i.e., by the back end of the penetrator).
Instead it's very interesting to find - for all perforating shots with still penetrator- the broken tip of the tool steel penetrators permanently welded on the plug (or target fragment) (Figure 49).

On the contrary, the cemented tungsten carbide penetrator is not welded to the plug (Figure 47b).

In one case we found also the brass case material welded to the plug (Figures 54 a. and c.) and we cannot see adiabatic shear bands on this component.

In the open literature this result is not described: neither the explosion welding of the steel penetrators, nor the behaviour of the tungsten carbide penetrator.

In some cases we have noted also an explosion welding between the penetrator and the plate even without the loss of the tip (Figures 38b and 58):
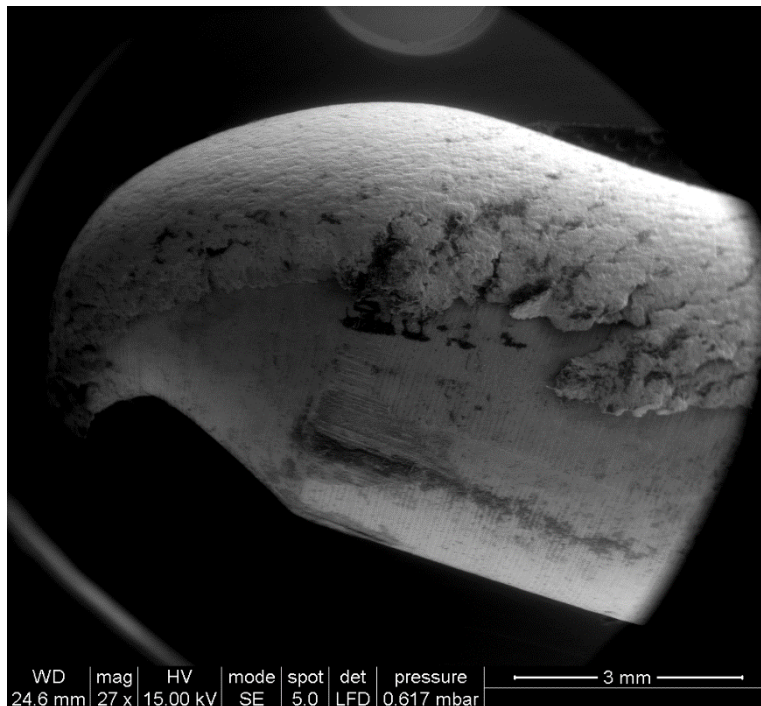
Figure 58: Explosion welding without loss of the tip

4.3   Adiabatic shear banding

From a microscopic point of view, all tool steel penetrators undergo adiabatic shear banding (Figures 54, 55 and 56), and this phenomenon is apparently responsible for:

- the welding between the penetrator and the plug, as evidenced by metallographic cross-section examination,
- the penetrator tip fracture, as evidenced by the fractographic examination (even if intergranular and ductile fracture also occur in limited areas, in particular in the 90MnCrV8 tool steel grade).

For both the behaviours described above, the amount of shear banding seems to be responsible, in fact, in the target plate material and in the three different penetrators, it is remarkably different: in particular, the HS6-5-2 tool steel grade exhibits the smaller amount of shear bands (much less than the adjacent target plate material), X153CrMoV12 have a

medium amount of band and the 90MnCrV8 grade the largest (much more than the target material).

From the above, it seems clear that the better piercing performance of the HS6-5-2 high speed steel can be related to the lower amount of energy spent in the penetrator deformation, due to adiabatic shear banding.

So, it can be identified as a correlation between the piercing efficiency of the steels and the amount of shear bands, as also it happens for the other materials.

Acknowledgements

Table of figures

87

References

1. Zukas, Jonas A., et al. "Impact dynamics". Journal of Applied Mechanics 50 (1983): 702;

2. Goldsmith, Werner. "Impact". Courier Corporation, 2001;

3. Backman, Marvin E., and Werner Goldsmith. "The mechanics of penetration of projectiles into targets" International Journal of Engineering Science 16.1 (1978): 1-99;

4. Zukas, J. A. "High velocity impact dynamics". John Wiley&Sons, New York. 1990;

5. Oscarson, John H., and Karl F. Graff. "Spall fracture and dynamic response of materials". No. BAT-197A-4-3. Battelle Memorial Inst. Columbus Labs, 1968.

6. Bürger, Daniel, et al. "Ballistic impact simulation of an armour-piercing projectile on hybrid ceramic/fiber reinforced composite armours.". International Journal of Impact Engineering 43 (2012): 63-77;

7. O'Keefe, John D., and Thomas J. Ahrens. "Impact and explosion crater ejecta, fragment size, and velocity". Icarus 62.2 (1985): 328-338;

8. Johnson, Gordon R., and William H. Cook. "A constitutive model and data for metals subjected to large strains, high strain rates and high temperatures". Proceedings of the 7th International Symposium on Ballistics. Vol. 21. 1983;

9. Johnson, Gordon R., and William H. Cook. "Fracture characteristics of three metals subjected to various strains, strain rates, temperatures and pressures" Engineering fracture mechanics 21.1 (1985): 31-48;

10. Ryu, Ho J., Soon H. Hong, and Woon H. Baek. "Microstructure and mechanical properties of mechanically alloyed and solid-state sintered tungsten heavy alloys." Materials Science and Engineering: A 291.1 (2000): 91-96;

11. Agency for Toxic Substances and Disease Registry: Public health statement Tungsten CAS 7440-33-7;

12. Chen, X. W., and G. Chen. "Experimental research on the penetration of tungsten-fiber/metallic-glass matrix composite material bullet into steel target." EPJ Web of Conferences. Vol. 26. EDP Sciences, 2012;

13. Cantaluppi, Chiara, and Sandro Degetto. "Civilian and military uses of depleted uranium: environmental and health problems." Annali di Chimica 90.11/12 (2000): 665-676;

14. Miller, Alexandra C. "A Review of Depleted Uranium Biological Effects: In vivo Studies". ARMED FORCES RADIOBIOLOGY RESEARCH INST BETHESDA MD, 2010;

15. Peacock, H. B. "Pyrophoricity of uranium." Report No. WSRC-TR-92-106. Westinghouse Savannah River Co., Aiken, SC (United States), 1992;

16. Batra, R. C., and Z. Peng. "Development of shear bands in dynamic plane strain compression of depleted uranium and tungsten blocks." International journal of impact engineering 16.3 (1995): 375-395;

17. Elia F., "I principi fondamentali nella condotta delle operazioni militari". Centro Alti Studi per la Difesa;

18. Sprince, Nancy L., et al. "Respiratory disease in tungsten carbide production workers." CHEST Journal 86.4 (1984): 549-557;

19. European Union Regulation No. 348/2013, amending Annex XIV to European Community Regulation No. 1907/2006, concerning the Registration, Evaluation, Authorization and Restriction of Chemicals (REACH);

20. Edwards, M. R., and A. Mathewson. "The ballistic properties of tool steel as a potential improvised armor plate." International journal of impact engineering 19.4 (1997): 297-309;

21. Anderson Jr, Charles E., et al. "The influence of projectile hardness on ballistic performance." International journal of impact engineering 22.6 (1999): 619-632;

22. Paris, V., et al. "Fragmentation of armor piercing steel projectiles upon oblique perforation of steel plates." EPJ Web of Conferences. Vol. 26. EDP Sciences, 2012;

23. Leonard, Wendy. The Effect of Nose Shape on Depleted Uranium (DU) Long-Rod Penetrators. No. ARL-TR-1505. ARMY RESEARCH LAB ABERDEEN PROVING GROUND MD, 1997;

24. STANAG 2920 PPS (Edition 2): Ballistic test method for personal armor materials and combat clothing. 2003 NSA/0723-PPS/2920;

25. Anderson Jr, Charles E., et al. "The influence of projectile hardness on ballistic performance." International journal of impact engineering 22.6 (1999): 619-632.